

Communications in Applied Mathematics and Computational Science

**GLOBALY DIVERGENCE-FREE DG SCHEME
FOR IDEAL COMPRESSIBLE MHD**

DINSHAW S. BALSARA, RAKESH KUMAR
AND PRAVEEN CHANDRASHEKAR

vol. 16 no. 1

2021

GLOBALLY DIVERGENCE-FREE DG SCHEME FOR IDEAL COMPRESSIBLE MHD

DINSHAW S. BALSARA, RAKESH KUMAR AND PRAVEEN CHANDRASHEKAR

The high-accuracy solution of the MHD equations is of great interest in various fields of physics, mathematics, and engineering. Higher-order DG schemes offer low dissipation and dispersion as well as the ability to model complex geometries, which is very desirable in various applications. Numerical solution of the MHD equations is made challenging by the fact that the PDE system has an involution constraint. Therefore, we construct high-order, globally divergence-free DG schemes for compressible MHD. The modes of the fluid variables are collocated at the zones of the mesh; the magnetic field components and their higher-order modes are collocated at the faces of the mesh. The fluid equations are evolved using classical DG, while the magnetic fields are evolved using a novel DG-like approach, first proposed by Balsara and Käppeli (*J. Comput. Phys.* **336** (2017), 104–127). This DG-like method ensures the globally divergence-free evolution of the magnetic field.

The method is built around three building blocks. The first building block consists of a divergence-free reconstruction of the magnetic field. The second building block consists of a DG-like formulation of Faraday’s law that provides a weak-form interpretation of Stokes’ law (as opposed to traditional DG, which relies on Gauss’s law). To provide a physically consistent electric field for the update of Faraday’s law, we use the third building block, which consists of a multidimensional Riemann solver that is evaluated at the edges of the mesh. We recognize that the limiting of facial variables makes the design of the MHD limiter very different from the usual DG limiter. As a result, a limiter strategy is presented for DG schemes which retains the traditional DG limiting approach while building into it a positivity-enforcement step and a step that updates the facial modes in a constraint-preserving fashion. This limiter is crucial to the robust and physically consistent operation of our DG scheme for MHD even at high orders.

It is shown that our schemes meet their design accuracies at second, third, and fourth orders on smooth test problems. Several stringent test problems with complex flow features are presented, which are robustly handled by our DG method.

Balsara is the corresponding author.

MSC2020: 35L65, 35L67, 65M12, 65M60, 76W05.

Keywords: ideal compressible MHD, divergence-free, discontinuous Galerkin method.

1. Introduction

The magnetohydrodynamic (MHD) equations are widely used in astrophysics, space physics, plasma physics, fusion research, and several other application areas. In all of these areas, there is an emerging interest in the highly accurate solution of the MHD equations. Part of this interest stems from the fact that modern-day supercomputers have become fast enough to permit some realistic calculations. Another part of this interest stems from the fact that various fields of study are taking interest in MHD turbulence, and such studies require numerical schemes that have low dissipation and low dispersion error. Discontinuous Galerkin (DG) schemes [28; 27; 29] have been used very effectively in numerically driven research into fluid turbulence. It is, therefore, natural to want to develop DG schemes for numerical MHD. Balsara and Käppeli [13] ([BK] henceforth) designed DG schemes for MHD that satisfy the involution constraints that make computational MHD more intricate than computational fluid dynamics. In [BK], we focused on the von Neumann stability analysis and found that higher-order DG schemes for MHD would provide low dissipation and very isotropic propagation of waves. This paper is devoted to a study of globally constraint-preserving DG schemes for numerical MHD.

The MHD system consists of a coupling of the fluid equations with Maxwell's equations under a simplifying assumption. Eliminating the displacement current in Ampere's law also eliminates the role of fast moving waves. Under that simplification, only Faraday's law for the evolution of the magnetic field is retained. Furthermore, even Faraday's law is simplified so that in ideal MHD the electric field that participates in Faraday's law is based on a motional electromagnetic field. Faraday's law provides an involution constraint which ensures that the magnetic field remains globally divergence-free. This involution constraint is expressed in codes via mimetic schemes that use a Yee-type staggering of the magnetic and electric field [69]. Consequently, the magnetic field components are collocated at the faces of the mesh and the electric fields are collocated at the edges of the mesh. Several early efforts that predated higher-order Godunov methodology focused on retaining this staggering of variables [19; 37; 32]. In time, several effective Riemann solvers were developed for MHD which led to the development of higher-order Godunov schemes for MHD [20; 70; 71; 56; 21; 43; 51; 53; 40; 22; 66; 65; 34]. With the development of Riemann solvers, several second-order Godunov schemes were formulated which preserved the divergence constraint [31; 59; 18; 52; 41; 42; 4].

Going beyond second order has required several interesting innovations. Several advances were made in higher-order constraint-preserving reconstruction of magnetic fields [1; 2; 3; 10; 67] which ensure that we can start with the facially collocated magnetic field and obtain a divergence-free magnetic field on the interior of the mesh. Because the electric field is collocated at the edges of the mesh, it

has to be updated in an upwinded fashion in both the directions that are transverse to that edge. This led to the development of multidimensional Riemann solvers [4; 6; 7; 8; 12; 11; 16]. These two innovations, consisting of constraint-preserving reconstruction of vector fields and multidimensional Riemann solvers, opened the door to a logically complete description of numerical MHD. To achieve seamless higher-order timestepping, a third innovation in ADER (arbitrary derivatives in space and time) timestepping schemes was added which greatly simplified the accurate temporal evolution of MHD variables [35; 36; 17; 15]. The globally constraint-preserving DG scheme in [BK] is constructed from these building blocks. Globally divergence-free central DG schemes have been developed in [50; 49; 23], while [48; 68] make use of a locally divergence-free approach. There are also several methods for MHD in the finite-difference WENO framework that do not use a staggering of the variables and make use of a vector potential to ensure divergence-free constraint [57; 45; 46; 26], with positivity-enforcement [25] and curvilinear grids [24]. An E-CUSP scheme together with the CT approach of Balsara and Spicer was developed in [60] and a wavelet-based adaptive WENO with divergence cleaning in [33]. A globally divergence-free DG scheme was developed in [39] up to third-order accuracy using divergence-free reconstruction and multidimensional fluxes. A recent review of higher-order methods is available in [9].

In [BK], we focused on a globally constraint-preserving DG scheme for the induction equation. We found that higher-order DG schemes for MHD could provide low dissipation and very isotropic propagation of waves. Subsequent papers [14; 44] show that superlative DG schemes arise at fourth and higher orders. Therefore, the goal of this work is to document constraint-preserving DG schemes for MHD that go at least up to fourth order. The limiting of facial modes in the DG scheme also has to be done very delicately if the optimal accuracy of DG is to be retained. Building on a method in [10], we present such a limiting strategy.

The MHD equations are nonconvex and extremely nonlinear. Simulations of MHD flows can also have extremely strong shocks and very large magnetic fields. This has the result that the effectiveness of a DG scheme depends on nonlinear limiting and positivity preservation. This paper represents a complete implementation of the DG-like scheme that was analyzed in [BK] in that it includes all elements of a successful DG scheme that extends to all orders. An earlier paper by Fu et al. [39] also attempts to implement the DG-like method from [BK], but it has two major limitations. First, the method of Fu et al. [39] produces severely negative pressures as seen in their Figures 12(b) and 14(b). Those figures should be contrasted with Figures 13, top right, 14, top right, and 15, top right, from this paper, which show that a pressure-positive solution can be obtained for the same test problem. Second, the paper by Fu et al. [39] only addresses second and third order, for which the divergence-free reconstruction problem is trivial and analytically specified in [BK].

The major challenge arises at fourth and higher orders where the divergence-free reconstruction problem and its use in a DG-like scheme is nontrivial. In this paper we show that DG-like schemes at fourth order are achievable and that opens the door to even higher orders [44].

The rest of the paper is organized as follows. [Section 2](#) briefly documents the ideal MHD equations. [Section 3](#) describes the approximation spaces for the facially collocated magnetic fields and their higher-order DG moments. [Section 4](#) describes the globally divergence-free reconstruction that results from utilizing face-centered moments of the magnetic field as our primal variables. [Section 5](#) describes the evolutionary equations that result from imposing a DG-like update strategy on the face-centered magnetic field moments; it also describes the DG scheme used in the evolution of the zone-centered fluid variables. The treatment of numerical fluxes is described in [Section 6](#) and the limiting strategy is described in [Section 7](#). [Section 8](#) describes the identification of troubled cells and [Section 9](#) presents numerical results. [Section 10](#) draws some conclusions.

2. Ideal MHD equations

Let ρ and p be the density and pressure of the gas, \mathcal{E} the total energy per unit volume, $\mathbf{v} = (v_x, v_y, v_z)$ the gas velocity, and $\mathfrak{B} = (B_x, B_y, B_z)$ the magnetic field. The compressible ideal MHD equations can be written as a first-order system of conservation laws of the form

$$\frac{\partial \mathcal{U}}{\partial t} + \frac{\partial \mathcal{F}_x}{\partial x} + \frac{\partial \mathcal{F}_y}{\partial y} + \frac{\partial \mathcal{F}_z}{\partial z} = 0$$

where \mathcal{U} is the vector of conserved variables given by

$$\mathcal{U} = [\rho \ \rho v_x \ \rho v_y \ \rho v_z \ \mathcal{E} \ B_x \ B_y \ B_z]^\top$$

and $\mathcal{F}_x, \mathcal{F}_y, \mathcal{F}_z$ are the Cartesian components of the flux vector and are given by

$$\mathcal{F}_x = \begin{bmatrix} \rho v_x \\ P + \rho v_x^2 - \frac{1}{4\pi} B_x^2 \\ \rho v_x v_y - \frac{1}{4\pi} B_x B_y \\ \rho v_x v_z - \frac{1}{4\pi} B_x B_z \\ (\mathcal{E} + P)v_x - \frac{1}{4\pi} B_x(\mathbf{v} \cdot \mathfrak{B}) \\ 0 \\ v_x B_y - v_y B_x \\ v_x B_z - v_z B_x \end{bmatrix}, \quad \mathcal{F}_y = \begin{bmatrix} \rho v_y \\ \rho v_x v_y - \frac{1}{4\pi} B_x B_y \\ P + \rho v_y^2 - \frac{1}{4\pi} B_y^2 \\ \rho v_y v_z - \frac{1}{4\pi} B_y B_z \\ (\mathcal{E} + P)v_y - \frac{1}{4\pi} B_y(\mathbf{v} \cdot \mathfrak{B}) \\ v_y B_x - v_x B_y \\ 0 \\ v_y B_z - v_z B_y \end{bmatrix},$$

$$\mathcal{F}_z = \begin{bmatrix} \rho v_z \\ \rho v_x v_z - \frac{1}{4\pi} B_x B_z \\ \rho v_y v_z - \frac{1}{4\pi} B_y B_z \\ P + \rho v_z^2 - \frac{1}{4\pi} B_z^2 \\ (\mathcal{E} + P)v_z - \frac{1}{4\pi} B_z(\mathbf{v} \cdot \mathbf{B}) \\ v_z B_x - v_x B_z \\ v_z B_y - v_y B_z \\ 0 \end{bmatrix}$$

where

$$\mathbf{B} = (B_x, B_y, B_z), \quad P = p + \frac{1}{8\pi} |\mathbf{B}|^2,$$

and the total energy is given by

$$\mathcal{E} = \frac{p}{\gamma - 1} + \frac{1}{2} \rho |\mathbf{v}|^2 + \frac{1}{8\pi} |\mathbf{B}|^2.$$

The last three components of the above system are sometimes called the *induction equation* and can be written in vector form as

$$\frac{\partial \mathbf{B}}{\partial t} + \nabla \times \mathbf{E} = 0, \quad \mathbf{E} = -\mathbf{v} \times \mathbf{B}.$$

Since magnetic monopoles have not been observed in nature, we must ensure that $\nabla \cdot \mathbf{B} = 0$. Taking the divergence of the above equation and due to the presence of the curl operator, we have the constraint

$$\frac{\partial}{\partial t} \nabla \cdot \mathbf{B} = 0.$$

Hence, the induction equation ensures that this condition is automatically satisfied, provided it holds at the initial time. However, a numerical scheme has to be carefully designed to have this property and such schemes are called *constraint-preserving*. In the present work we consider the 2D case where the conservation law is of the form

$$\frac{\partial \mathcal{U}}{\partial t} + \frac{\partial \mathcal{F}_x}{\partial x} + \frac{\partial \mathcal{F}_y}{\partial y} = 0 \tag{1}$$

where $\mathcal{U}, \mathcal{F}_x, \mathcal{F}_y$ are defined as before and these are functions of only the x, y coordinates. The divergence constraint is now based on the 2D divergence defined as

$$\mathbf{B} = (B_x, B_y), \quad \nabla \cdot \mathbf{B} = \frac{\partial B_x}{\partial x} + \frac{\partial B_y}{\partial y} = 0.$$

The electric field has only one component $E_z = v_y B_x - v_x B_y$, and we write the induction equation for only the x, y components

$$\frac{\partial B_x}{\partial t} + \frac{\partial E_z}{\partial y} = 0, \quad \frac{\partial B_y}{\partial t} - \frac{\partial E_z}{\partial x} = 0. \quad (2)$$

The numerical strategy we develop below involves a standard DG scheme for the conservation law (1) and a constraint-preserving DG scheme for the induction equation (2). The magnetic field components are present in the \mathcal{U} variables also, and we use this provisional update to devise a limiter strategy, while the actual magnetic field update is achieved using a constraint-preserving DG scheme applied to the induction equation.

3. Approximation spaces

We would like to approximate the vector field \mathbf{B} such that its divergence is zero inside the cell. The approach we take to do this is to use the reconstruction scheme of Balsara [3], which makes use of known values of the normal component of \mathbf{B} on the faces of the cell and then reconstructs the vector field inside the cell by enforcing appropriate constraints on its divergence.

Let k be the degree of polynomials used to approximate the normal components on the faces. We map each cell to the reference cell $[-1/2, +1/2] \times [-1/2, +1/2]$ with coordinates (ξ, η) and construct the basis functions on the reference cell. Thus, on the two vertical faces of a cell, the normal component which is the x component is given by

$$B_x^\pm(\eta) = \sum_{j=0}^k a_j^\pm \phi_j(\eta) \in \mathbb{P}_k(\eta)$$

while on the two horizontal faces, the corresponding normal component is given by

$$B_y^\pm(\xi) = \sum_{j=0}^k b_j^\pm \phi_j(\xi) \in \mathbb{P}_k(\xi).$$

The basis functions for $\mathbb{P}_k(\xi)$ are taken to be mutually orthogonal polynomials given by

$$\phi_0(\xi) = 1, \quad \phi_1(\xi) = \xi, \quad \phi_2(\xi) = \xi^2 - \frac{1}{12}, \quad \phi_3(\xi) = \xi^3 - \frac{3}{20}\xi, \quad \phi_4(\xi) = \xi^4 - \frac{3}{14}\xi^2 + \frac{3}{560}.$$

The orthogonality property implies that

$$\int_{-1/2}^{+1/2} B_x^\pm(\eta) d\eta = a_0^\pm, \quad \int_{-1/2}^{+1/2} B_y^\pm(\xi) d\xi = b_0^\pm$$

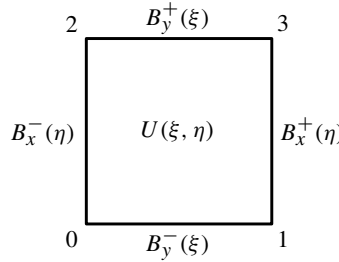


Figure 1. Storage of solution variables: normal components of \mathbf{B} are stored on faces, and hydrodynamic variables, including B_z , are stored inside the cell.

so that a_0 and b_0 are the average values of the corresponding normal components on the faces. For later use, let us define

$$m_i = \int_{-1/2}^{+1/2} \phi_i^2(\xi) d\xi,$$

which are the diagonal entries of the 1D mass matrix associated with the orthogonal polynomials. The variables \mathcal{U} will be approximated inside each cell by 2D polynomials of degree k usually denoted as $\mathbb{P}_k(\xi, \eta)$ and given by

$$\mathcal{U}(\xi, \eta) = \sum_{i=0}^{N(k)-1} \mathcal{U}_i \Phi_i(\xi, \eta), \quad N(k) = \frac{1}{2}(k+1)(k+2), \quad (3)$$

where $\Phi_0(\xi, \eta) = 1$ and

$$\begin{aligned} \Phi_1(\xi, \eta) &= \phi_1(\xi), & \Phi_2(\xi, \eta) &= \phi_1(\eta) & \Phi_3(\xi, \eta) &= \phi_2(\xi), \\ \Phi_4(\xi, \eta) &= \phi_1(\xi)\phi_1(\eta), & \Phi_5(\xi, \eta) &= \phi_2(\eta), & \Phi_6(\xi, \eta) &= \phi_3(\xi), \\ \Phi_7(\xi, \eta) &= \phi_2(\xi)\phi_1(\eta), & \Phi_8(\xi, \eta) &= \phi_1(\xi)\phi_2(\eta), & \Phi_9(\xi, \eta) &= \phi_3(\eta). \end{aligned}$$

The above 2D basis functions are mutually orthogonal with respect to the inner product on the reference cell. [Figure 1](#) shows the location of the above solution polynomials. The set \mathcal{U} contains the magnetic field components B_x , B_y , but these are *not independent variables*; instead they will be obtained via a divergence-free reconstruction process which is described below. These magnetic components will only be used to perform some limiting step. By Gauss's theorem,

$$0 = \int_C \nabla \cdot \mathbf{B} dx dy = \int_{\partial C} \mathbf{B} \cdot \mathbf{n} ds,$$

which implies that

$$(a_0^+ - a_0^-) \Delta y + (b_0^+ - b_0^-) \Delta x = 0. \quad (4)$$

The above constraint will be satisfied by the initial condition, and the update scheme we devise will ensure that it is satisfied at future times also.

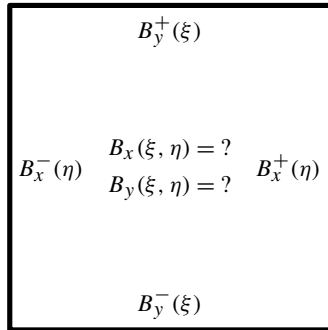


Figure 2. Divergence-free reconstruction problem: given normal components on faces, find the field inside the cell.

In a cell (see [Figure 2](#)) using the information of B_x^\pm, B_y^\pm , we have to reconstruct $\mathbf{B} = \mathbf{B}(\xi, \eta)$ inside each cell such that the following conditions are satisfied:

- (1) The normal components of $\mathbf{B}(\xi, \eta)$ match the known values on the faces:

$$B_x(\pm 1/2, \eta) = B_x^\pm(\eta), \quad \eta \in [-1/2, +1/2],$$

$$B_y(\xi, \pm 1/2) = B_y^\pm(\xi), \quad \xi \in [-1/2, +1/2].$$

- (2) The divergence of \mathbf{B} is zero:

$$\nabla \cdot \mathbf{B}(\xi, \eta) = 0, \quad \xi, \eta \in [-1/2, +1/2].$$

Since we directly approximate the normal component on the faces, the continuity of normal component of \mathbf{B} is guaranteed since both cells adjacent to a face share the same value of the normal component. The precise form of the polynomial $\mathbf{B}(\xi, \eta)$ and the solution of the above reconstruction problem at various orders is given in the next section.

4. Reconstruction of \mathbf{B} inside a cell

Given the normal components on the faces of the mesh, we can reconstruct the vector field \mathbf{B} inside the cell in a divergence-free manner. We assume that \mathbf{B} has a certain polynomial structure which will be given at various orders below. In each case, the assumed polynomial form contains the space $\mathbb{P}_k(\xi, \eta)$ of complete polynomials of degree k which is necessary to obtain the good approximation property, an error of $O(h^{k+1})$. We will see that the polynomial space for \mathbf{B} has to be slightly larger than \mathbb{P}_k in order to incorporate the conditions for divergence-conforming approximation.

4.1. Reconstruction at degree $k = 0$. In this case we have constant approximation on the faces for the normal components, i.e.,

$$B_x^\pm(\eta) = a_0^\pm, \quad B_y^\pm(\xi) = b_0^\pm,$$

$a_{00} = \frac{1}{2}(a_0^- + a_0^+) + \frac{1}{12}(b_1^+ - b_1^-) \frac{\Delta x}{\Delta y}$	$b_{00} = \frac{1}{2}(b_0^- + b_0^+) + \frac{1}{12}(a_1^+ - a_1^-) \frac{\Delta y}{\Delta x}$
$a_{10} = a_0^+ - a_0^-$	$b_{10} = \frac{1}{2}(b_1^- + b_1^+)$
$a_{01} = \frac{1}{2}(a_1^- + a_1^+)$	$b_{01} = b_0^+ - b_0^-$
$a_{20} = \frac{1}{2}(b_1^- - b_1^+) \frac{\Delta x}{\Delta y}$	$b_{02} = \frac{1}{2}(a_1^- - a_1^+) \frac{\Delta y}{\Delta x}$
$a_{11} = a_1^+ - a_1^-$	$b_{11} = b_1^+ - b_1^-$

Table 1. Divergence-free reconstruction for $k = 1$.

and the vector field inside the cell is of the form

$$B_x(\xi, \eta) = a_{00} + a_{10}\phi_1(\xi), \quad B_y(\xi, \eta) = b_{00} + b_{01}\phi_1(\eta),$$

which has a dimension of four. The solution of the reconstruction problem is given by

$$a_{00} = \frac{1}{2}(a_0^- + a_0^+), \quad b_{00} = \frac{1}{2}(b_0^- + b_0^+), \quad a_{10} = a_0^+ - a_0^-, \quad b_{01} = b_0^+ - b_0^-.$$

This is the lowest-order approximation, and we observe that the functions are not piecewise constant, unlike in usual DG schemes where the lowest-order approximations comprise piecewise constant functions. This is due to the need to ensure the continuity conditions on the normal components. The reconstruction is completely determined by the solution given on the faces.

4.2. Reconstruction at degree $k = 1$. The face solution is a polynomial of degree one of the form

$$B_x^\pm(\eta) = a_0^\pm + a_1^\pm\phi_1(\eta), \quad B_x^\pm(\eta) = b_0^\pm + b_1^\pm\phi_1(\xi).$$

The vector field inside the cell is taken to be of the form

$$B_x(\xi, \eta) = a_{00} + a_{10}\phi_1(\xi) + a_{01}\phi_1(\eta) + a_{20}\phi_2(\xi) + a_{11}\phi_1(\xi)\phi_1(\eta),$$

$$B_y(\xi, \eta) = b_{00} + b_{10}\phi_1(\xi) + b_{01}\phi_1(\eta) + b_{11}\phi_1(\xi)\phi_1(\eta) + b_{02}\phi_2(\eta),$$

which has a dimension of 10. The solution of the divergence-free reconstruction is given in [Table 1](#). The reconstruction is completely determined by the solution given on the faces.

4.3. Reconstruction at degree $k = 2$. The face solution is a polynomial of degree two and has the form

$$B_x^\pm(\eta) = a_0^\pm + a_1^\pm\phi_1(\eta) + a_2^\pm\phi_2(\eta), \quad B_y^\pm(\xi) = b_0^\pm + b_1^\pm\phi_1(\xi) + b_2^\pm\phi_2(\xi).$$

$a_{00} = \frac{1}{2}(a_0^- + a_0^+) + \frac{1}{12}(b_1^+ - b_1^-) \frac{\Delta x}{\Delta y}$	$b_{00} = \frac{1}{2}(b_0^- + b_0^+) + \frac{1}{12}(a_1^+ - a_1^-) \frac{\Delta y}{\Delta x}$
$a_{10} = a_0^+ - a_0^- + \frac{1}{30}(b_2^+ - b_2^-) \frac{\Delta x}{\Delta y}$	$b_{01} = b_0^+ - b_0^- + \frac{1}{30}(a_2^+ - a_2^-) \frac{\Delta y}{\Delta x}$
$a_{11} = a_1^+ - a_1^-$	$b_{11} = b_1^+ - b_1^-$
$a_{02} = \frac{1}{2}(a_2^- + a_2^+)$	$b_{20} = \frac{1}{2}(b_2^- + b_2^+)$
$a_{20} = -\frac{1}{2}(b_1^+ - b_1^-) \frac{\Delta x}{\Delta y}$	$b_{02} = -\frac{1}{2}(a_1^+ - a_1^-) \frac{\Delta y}{\Delta x}$
$a_{12} = a_2^+ - a_2^-$	$b_{03} = -\frac{1}{3}(a_2^+ - a_2^-) \frac{\Delta y}{\Delta x}$
$a_{30} = -\frac{1}{3}(b_2^+ - b_2^-) \frac{\Delta x}{\Delta y}$	$b_{21} = b_2^+ - b_2^-$
$a_{01} = \frac{1}{2}(a_1^- + a_1^+)$	$b_{10} = \frac{1}{2}(b_1^- + b_1^+)$

Table 2. Divergence-free reconstruction for $k = 2$.

The field inside the cell is approximated by

$$B_x(\xi, \eta) = a_{00} + a_{10}\phi_1(\xi) + a_{01}\phi_1(\eta) + a_{20}\phi_2(\xi) + a_{11}\phi_1(\xi)\phi_1(\eta) + a_{02}\phi_2(\eta) \\ + a_{30}\phi_3(\xi) + a_{12}\phi_1(\xi)\phi_2(\eta),$$

$$B_y(\xi, \eta) = b_{00} + b_{10}\phi_1(\xi) + b_{01}\phi_1(\eta) + b_{20}\phi_2(\xi) + b_{11}\phi_1(\xi)\phi_1(\eta) + b_{02}\phi_2(\eta) \\ + b_{21}\phi_2(\xi)\phi_1(\eta) + b_{03}\phi_3(\eta),$$

which has a dimension of 16. The solution of the divergence-free reconstruction is in [Table 2](#) and is completely determined by the solution given on the faces.

4.4. Reconstruction at degree $k = 3$. The face solution is a polynomial of degree three and has the form

$$B_x^\pm(\eta) = a_0^\pm\phi_0(\eta) + a_1^\pm\phi_1(\eta) + a_2^\pm\phi_2(\eta) + a_3^\pm\phi_3(\eta), \\ B_y^\pm(\xi) = b_0^\pm\phi_0(\xi) + b_1^\pm\phi_1(\xi) + b_2^\pm\phi_2(\xi) + b_3^\pm\phi_3(\xi).$$

The vector field has the form

$$B_x(\xi, \eta) = a_{00} + a_{10}\phi_1(\xi) + a_{01}\phi_1(\eta) + a_{20}\phi_2(\xi) + a_{11}\phi_1(\xi)\phi_1(\eta) + a_{02}\phi_2(\eta) \\ + a_{30}\phi_3(\xi) + a_{21}\phi_2(\xi)\phi_1(\eta) + a_{12}\phi_1(\xi)\phi_2(\eta) + a_{03}\phi_3(\eta) \\ + a_{40}\phi_4(\xi) + a_{13}\phi_1(\xi)\phi_3(\eta),$$

$$B_y(\xi, \eta) = b_{00} + b_{10}\phi_1(\xi) + b_{01}\phi_1(\eta) + b_{20}\phi_2(\xi) + b_{11}\phi_1(\xi)\phi_1(\eta) + b_{02}\phi_2(\eta) \\ + b_{30}\phi_3(\xi) + b_{21}\phi_2(\xi)\phi_1(\eta) + b_{12}\phi_1(\xi)\phi_2(\eta) + b_{03}\phi_3(\eta) \\ + b_{31}\phi_3(\xi)\phi_1(\eta) + b_{04}\phi_4(\eta),$$

which has a dimension of 24. At this order, the reconstruction problem cannot be solved using the facial information alone since there is one extra unknown, i.e., one equation fewer than the number of unknown coefficients. Hence, we assume that

$a_{00} = \frac{1}{2}(a_0^- + a_0^+) + \frac{1}{12}(b_1^+ - b_1^-) \frac{\Delta x}{\Delta y}$	$b_{00} = \frac{1}{2}(b_0^- + b_0^+) + \frac{1}{12}(a_1^+ - a_1^-) \frac{\Delta y}{\Delta x}$
$a_{10} = a_0^+ - a_0^- + \frac{1}{30}(b_2^+ - b_2^-) \frac{\Delta x}{\Delta y}$	$b_{01} = b_0^+ - b_0^- + \frac{1}{30}(a_2^+ - a_2^-) \frac{\Delta y}{\Delta x}$
$a_{20} = -\frac{1}{2}(b_1^+ - b_1^-) \frac{\Delta x}{\Delta y} + \frac{3}{140}(b_3^+ - b_3^-) \frac{\Delta x}{\Delta y}$	$b_{02} = -\frac{1}{2}(a_1^+ - a_1^-) \frac{\Delta y}{\Delta x} + \frac{3}{140}(a_3^+ - a_3^-) \frac{\Delta y}{\Delta x}$
$a_{30} = -\frac{1}{3}(b_2^+ - b_2^-) \frac{\Delta x}{\Delta y}$	$b_{30} = \frac{1}{2}(b_3^- + b_3^+)$
$a_{03} = \frac{1}{2}(a_3^- + a_3^+)$	$b_{03} = -\frac{1}{3}(a_2^+ - a_2^-) \frac{\Delta y}{\Delta x}$
$a_{12} = a_2^+ - a_2^-$	$b_{21} = b_2^+ - b_2^-$
$a_{40} = -\frac{1}{4}(b_3^+ - b_3^-) \frac{\Delta x}{\Delta y}$	$b_{31} = b_3^+ - b_3^-$
$a_{13} = a_3^+ - a_3^-$	$b_{04} = -\frac{1}{4}(a_3^+ - a_3^-) \frac{\Delta y}{\Delta x}$
$a_{02} = \frac{1}{2}(a_2^- + a_2^+)$	$b_{20} = \frac{1}{2}(b_2^- + b_2^+)$
$a_{11} = a_1^+ - a_1^-$	$b_{11} = b_1^+ - b_1^-$
$a_{01} = \frac{1}{1+\Delta y/\Delta x} [r_1 \frac{\Delta y}{\Delta x} + r_2 - \omega]$	$b_{10} = \omega + a_{01}$
$a_{21} = 6(r_1 - a_{01})$	$b_{12} = 6(r_2 - b_{10})$

Table 3. Divergence-free reconstruction for $k = 3$.

the value of $\omega = b_{10} - a_{01}$ is given so that we have a 25-dimensional approximation space. Define

$$r_1 = \frac{1}{2}(a_1^- + a_1^+), \quad r_2 = \frac{1}{2}(b_1^- + b_1^+).$$

Then the solution of the divergence-free reconstruction is given in [Table 3](#). At fourth order and above, the divergence-free reconstruction cannot be performed using face solution alone and we have to introduce extra information from the cell solution like the quantity ω introduced above, which is now an additional degree of freedom which will be evolved in time using the induction equation. The quantity ω is related to the curl of the magnetic field (see [\(7\)](#)) which shows that it measures the circulation of the magnetic field around the cell. Specifying this quantity to complete the reconstruction of the magnetic field vector seems natural and reminds us of the Helmholtz decomposition of a vector field into a curl-free part and a divergence-free part. Beyond fourth order, we will require still more additional information to perform the reconstruction and the reader is referred to [\[44\]](#) for additional details including the fifth-order approximation.

5. Numerical scheme

The basic unknowns in our scheme are the polynomials approximating the normal component of \mathbf{B} on the cell faces and the polynomials approximating the hydrodynamic variables and B_z inside the cells. At fourth order we have an additional variable ω stored inside each cell. This is illustrated in [Figure 3](#). We will first devise

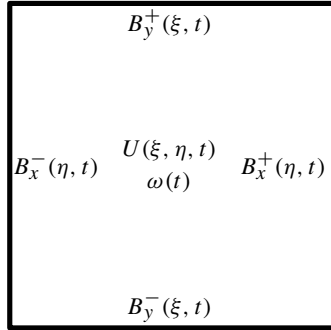


Figure 3. Storage of solution variables; ω is required only at fourth order ($k = 3$).

semidiscrete DG schemes for all these quantities using the weak formulation of the hydrodynamic conservation laws and the induction equation, leading to a set of ODEs, which can then be integrated forward in time using a Runge–Kutta scheme.

5.1. Discontinuous Galerkin method for B on the faces. The normal component of \mathbf{B} has been approximated on the faces of our mesh using 1D polynomials of degree $k \geq 0$, and we want to construct a numerical scheme to evolve these values forward in time. If we observe the equation governing B_x , we see that it evolves only due to the y derivative of the electric field E_z . Restricting ourselves to a vertical face, we see that we have a 1D PDE for B_x which can be discretized using a 1D DG scheme applied on the face. Multiplying by a test function $\phi_i(\eta)$ and integrating by parts yields

$$\int_{-1/2}^{+1/2} \frac{\partial B_x}{\partial t} \phi_i \, d\eta - \frac{1}{\Delta y} \int_{-1/2}^{+1/2} \widehat{E}_z \frac{d\phi_i}{d\eta} \, d\eta + \frac{1}{\Delta y} [\widetilde{E}_z \phi_i] = 0, \quad 0 \leq i \leq k,$$

where \widehat{E}_z appearing in the face integral is obtained from a 1D Riemann solver and \widetilde{E}_z is obtained from a multidimensional Riemann solver. The face integral is computed using $(k + 1)$ -point Gauss–Legendre quadrature, which results in the semidiscrete scheme, for $i = 0, 1, \dots, k$,

$$m_i \frac{da_i}{dt} - \frac{1}{\Delta y} \sum_q \widehat{E}_z(\eta_q) \frac{d\phi_i}{d\eta}(\eta_q) \omega_q + \frac{1}{\Delta y} [\widetilde{E}_z(\tfrac{1}{2}) \phi_i(\tfrac{1}{2}) - \widetilde{E}_z(-\tfrac{1}{2}) \phi_i(-\tfrac{1}{2})] = 0. \quad (5)$$

Similarly on the horizontal faces, using a test function $\phi_i(\xi)$, the DG scheme for B_y is given by

$$\int_{-1/2}^{+1/2} \frac{\partial B_y}{\partial t} \phi_i \, d\xi + \frac{1}{\Delta x} \int_{-1/2}^{+1/2} \widehat{E}_z \frac{d\phi_i}{d\xi} \, d\xi - \frac{1}{\Delta x} [\widetilde{E}_z \phi_i] = 0, \quad 0 \leq i \leq k.$$

Using $(k+1)$ -point Gauss–Legendre quadrature on the face, we obtain the semidiscrete scheme, for $i = 0, 1, \dots, k$,

$$m_i \frac{db_i}{dt} + \frac{1}{\Delta x} \sum_q \widehat{E}_z(\xi_q) \frac{d\phi_i}{d\xi}(\xi_q) \omega_q - \frac{1}{\Delta x} [\widetilde{E}_z\left(\frac{1}{2}\right)\phi_i\left(\frac{1}{2}\right) - \widetilde{E}_z\left(-\frac{1}{2}\right)\phi_i\left(-\frac{1}{2}\right)] = 0. \quad (6)$$

5.2. Fourth-order scheme for \mathbf{B} . At fourth order of accuracy ($k = 3$), the normal components stored on the faces do not completely determine the divergence-free reconstruction of \mathbf{B} inside the cell. We have to specify ω as an additional information so that the reconstruction problem can be solved, which is defined as

$$\omega = b_{10} - a_{01} = 12 \int_{-1/2}^{+1/2} \int_{-1/2}^{+1/2} (B_y \xi - B_x \eta) d\xi d\eta. \quad (7)$$

Using the induction equation, a dynamical equation for ω can be obtained as

$$\begin{aligned} \frac{d\omega}{dt} &= 12 \int_{-1/2}^{+1/2} \int_{-1/2}^{+1/2} \left(\frac{\partial B_y}{\partial t} \xi - \frac{\partial B_x}{\partial t} \eta \right) d\xi d\eta \\ &= 12 \int_{-1/2}^{+1/2} \int_{-1/2}^{+1/2} \left(\frac{1}{\Delta x} \frac{\partial E_z}{\partial \xi} \xi + \frac{1}{\Delta y} \frac{\partial E_z}{\partial \eta} \eta \right) d\xi d\eta. \end{aligned}$$

Performing an integration by parts in the last two terms, and using a numerical flux on the faces which is based on a 1D Riemann solver, we obtain a semidiscrete DG scheme

$$\begin{aligned} \frac{d\omega}{dt} &= \frac{12}{\Delta x} \left[\frac{1}{2} \int_{-1/2}^{+1/2} \widehat{E}_z^{x-} d\eta + \frac{1}{2} \int_{-1/2}^{+1/2} \widehat{E}_z^{x+} d\eta - \int_{-1/2}^{+1/2} \int_{-1/2}^{+1/2} E_z d\xi d\eta \right] \\ &\quad + \frac{12}{\Delta y} \left[\frac{1}{2} \int_{-1/2}^{+1/2} \widehat{E}_z^{y-} d\xi + \frac{1}{2} \int_{-1/2}^{+1/2} \widehat{E}_z^{y+} d\xi - \int_{-1/2}^{+1/2} \int_{-1/2}^{+1/2} E_z d\xi d\eta \right] \end{aligned}$$

where the superscripts $x-$ and $x+$ denote the left and right faces of the cell, and $y-$ and $y+$ denote the bottom and top faces of the cell, and the fluxes \widehat{E}_z appearing in the face integrals are obtained from the 1D Riemann solver which is identical to what is used in the face equations in the previous section. The face integrals are computed with $(k+1)$ -point Gauss–Legendre quadrature, and the cell integral is computed using the tensor product of $(k+1)$ -point Gauss–Legendre quadrature.

5.3. Discontinuous Galerkin method for \mathcal{U} inside cells. The hydrodynamic variables and B_z which are grouped into the variable \mathcal{U} are approximated by $\mathbb{P}_k(\xi, \eta)$ polynomials inside each cell. The magnetic field components B_x, B_y are also present in this set, but these values are initialized using the divergence-free reconstruction. We will apply a standard DG scheme to the system of conservation laws (1); multiplying this equation by a test function Φ_i and performing an integration by

parts over one cell, we get

$$\begin{aligned} \int_{-1/2}^{+1/2} \int_{-1/2}^{+1/2} \frac{\partial \mathcal{U}}{\partial t} \Phi_i(\xi, \eta) d\xi d\eta - \int_{-1/2}^{+1/2} \int_{-1/2}^{+1/2} \left[\frac{1}{\Delta x} \mathcal{F}_x \frac{\partial \Phi_i}{\partial \xi} + \frac{1}{\Delta y} \mathcal{F}_y \frac{\partial \Phi_i}{\partial \eta} \right] d\xi d\eta \\ + \frac{1}{\Delta x} \int_{-1/2}^{+1/2} \widehat{\mathcal{F}}_x^+ \Phi_i\left(\frac{1}{2}, \eta\right) d\eta - \frac{1}{\Delta x} \int_{-1/2}^{+1/2} \widehat{\mathcal{F}}_x^- \Phi_i\left(-\frac{1}{2}, \eta\right) d\eta \\ + \frac{1}{\Delta y} \int_{-1/2}^{+1/2} \widehat{\mathcal{F}}_y^+ \Phi_i\left(\xi, \frac{1}{2}\right) d\xi - \frac{1}{\Delta y} \int_{-1/2}^{+1/2} \widehat{\mathcal{F}}_y^- \Phi_i\left(\xi, -\frac{1}{2}\right) d\xi = 0 \end{aligned}$$

where the test functions $\{\Phi_i, i = 0, 1, \dots, N(k) - 1\}$ are the basis functions of $\mathbb{P}_k(\xi, \eta)$, $\widehat{\mathcal{F}}_x^-, \widehat{\mathcal{F}}_x^+$ are the numerical fluxes on the left and right faces obtained from the 1D Riemann solver, and $\widehat{\mathcal{F}}_y^-, \widehat{\mathcal{F}}_y^+$ are the numerical fluxes on bottom and top faces obtained from the 1D Riemann solver. The integral inside the cell is evaluated using a tensor product of $(k + 1)$ -point Gauss–Legendre quadrature while the face integrals are evaluated using $(k + 1)$ -point Gauss–Legendre quadrature.

5.4. Compatibility condition. We have completely specified the update procedure for all the variables. To solve the reconstruction problem, we must ensure that the compatibility condition (4) will be satisfied by the solution at future times also, assuming that it is satisfied at the initial time. To verify this property, we consider one cell and look at the evolution equations for a_0^\pm, b_0^\pm on the faces of this cell. From (5) and (6) and with reference to Figure 1, we have

$$\begin{aligned} \frac{da_0^-}{dt} + \frac{(\tilde{E}_z)_2 - (\tilde{E}_z)_0}{\Delta y} &= 0, & \frac{da_0^+}{dt} + \frac{(\tilde{E}_z)_3 - (\tilde{E}_z)_1}{\Delta y} &= 0, \\ \frac{db_0^-}{dt} - \frac{(\tilde{E}_z)_1 - (\tilde{E}_z)_0}{\Delta x} &= 0, & \frac{db_0^+}{dt} - \frac{(\tilde{E}_z)_3 - (\tilde{E}_z)_2}{\Delta x} &= 0. \end{aligned}$$

Hence,

$$\begin{aligned} \frac{d}{dt} [(a_0^+ - a_0^-) \Delta y + (b_0^+ - b_0^-) \Delta x] &= (\tilde{E}_z)_3 - (\tilde{E}_z)_1 - (\tilde{E}_z)_2 + (\tilde{E}_z)_0 \\ &\quad - (\tilde{E}_z)_3 + (\tilde{E}_z)_2 + (\tilde{E}_z)_1 - (\tilde{E}_z)_0 \\ &= 0. \end{aligned}$$

The key property that leads to the above compatibility condition is the use of a unique numerical flux to estimate the electric field E_z at the vertices of the mesh, which is obtained from a multidimensional Riemann solver.

6. Numerical fluxes

A major component of the DG scheme is the specification of numerical fluxes required on the faces and vertices of the cells. These fluxes are determined by approximate solution of 1D and 2D Riemann problems. On the cell faces, we have

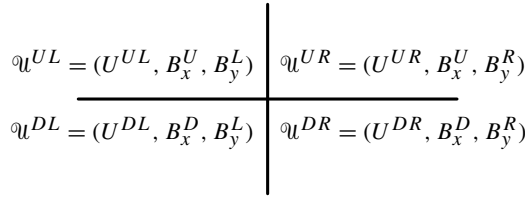


Figure 4. Four states of a 2D Riemann problem.

a 1D Riemann problem since the solution is possibly discontinuous. Let us define $\mathbf{U} = (\rho, \rho\mathbf{v}, \mathcal{E}, B_z)$, which is obtained from the set of conserved variables \mathcal{U} . The remaining components of the magnetic field B_x, B_y come from their polynomial expansions based on divergence-free reconstruction. For example at a vertical cell face, we have the left state $(\mathbf{U}^L, B_x, B_y^L)$ and a right state $(\mathbf{U}^R, B_x, B_y^R)$. Note that B_x , which is the normal component on a vertical face, has the same value on both sides since this component is directly approximated on the face and hence we have a unique value. The tangential component B_y is obtained by the divergence-free reconstruction in the two cells adjacent to the vertical face and can be discontinuous. We now have the two conserved state variables $\mathcal{U}^L = \mathcal{U}(\mathbf{U}^L, B_x, B_y^L)$ and $\mathcal{U}^R = \mathcal{U}(\mathbf{U}^R, B_x, B_y^R)$ and let $\widehat{\mathcal{F}}_x$ denote the numerical flux obtained by solving the 1D MHD Riemann problem corresponding to these two states. From this flux we can obtain the electric field that is required for the integrals on the cell faces:

$$\widehat{E}_z = -(\widehat{\mathcal{F}}_x)_7.$$

Similarly, at any horizontal face, we have the bottom state $\mathcal{U}^D = \mathcal{U}(\mathbf{U}^D, B_x^D, B_y)$ and top state $\mathcal{U}^U = \mathcal{U}(\mathbf{U}^U, B_x^U, B_y)$, where we now see that the normal component B_y is continuous. The solution of the 1D MHD Riemann problem with the two states $\mathcal{U}^D, \mathcal{U}^U$ yields the numerical flux $\widehat{\mathcal{F}}_y$ from which we obtain the fluxes required for our DG scheme and the electric field is given by

$$\widehat{E}_z = (\widehat{\mathcal{F}}_y)_6.$$

Finally, we need to specify the electric field \widetilde{E}_z at the vertices of the cells. At any vertex, we have four states that come together giving rise to a 2D Riemann problem as shown in [Figure 4](#). The solution of the 2D Riemann problem yields the fluxes $\mathcal{F}_x^{**}, \mathcal{F}_y^{**}$ from which the electric field at the vertex is obtained as

$$\widehat{E}_z = \frac{1}{2}[-(\mathcal{F}_x^{**})_7 + (\mathcal{F}_y^{**})_6].$$

The Riemann solvers are based on HLL-type solvers, and for more details on the 1D and 2D Riemann solvers, the reader is requested to consult [6; 10; 11; 15].

7. Limiting strategy for DG MHD

While the MHD system is an extension of the Euler system, it is even more strongly nonlinear than the Euler system. The Euler fluxes are homogeneous of degree one in the conserved variables;¹ the same is not the case for MHD. The MHD system is also nonconvex, while the Euler system is convex at least for simple equations of state. As a result, it is entirely reasonable to expect that the DG limiting strategies that have been developed in the context of Euler flows [72] might fall short for MHD flows. For example, limiting in the conserved variables is sufficient for Euler flow whereas it often proves inadequate for MHD flow.

For most Euler flow test problems one does not need to enforce positivity. However, for some extreme test problems involving the Euler equations, the velocity can become large enough that an evaluation of the pressure from the total energy density can return a negative value. In such situations, it is customary to enforce positivity in the DG scheme [72; 5]. However, for several common MHD flow simulations, the evaluation of the pressure from the total energy density can return a negative value because the magnetic field might have become very large in the zone being considered. A more stringent pressure positivity-enforcement is then called for within the context of numerical MHD flows [5]. Since the pressure positivity seeks to curtail the higher-order reconstruction that has been obtained by the limiter, the incorporation of a pressure positivity step should be considered integral to MHD limiting. We also see that the pressure positivity step should be applied after the limiting step. We will design a limiting strategy that integrates positivity-enforcement with limiting, as mentioned in this paragraph.

While the above two paragraphs argue that the limiting of MHD codes has to be rather stringent, it should also be sensitively implemented so as to retain three desirable attributes. First and foremost, the limiter should not destroy the order property. Second, in order to be economical, the limiting of the facially collocated magnetic field modes should leverage the rather expensive zone-centered limiting. Third, by the end of the limiting step, we should have a reconstructed divergence-free magnetic field within each zone that is consistent with the nonlinearly hybridized moments of the magnetic field components that reside in the faces of the mesh. Note that the facial limiting strategy can change the higher modes associated with the facially collocated components of the magnetic field. However, in order to keep the magnetic field divergence-free in an integral sense, it cannot change the facially averaged mean magnetic field components. In this work, we use TVD/TVB-type limiters which are well developed for hyperbolic systems of conservation laws, though they may not strictly retain accuracy unless the TVB parameter is chosen

¹That is, $\mathbf{F}(\alpha \mathbf{U}) = \alpha \mathbf{F}(\mathbf{U})$ for any α , where \mathbf{F} is any flux component and \mathbf{U} is any physically viable state.

carefully. We defer the development of a WENO-type limiter for MHD to a future work and instead use TVD/TVB-type limiters in this work.

To facilitate the implementation of limiters in DG codes for MHD, we will describe our limiting strategy in steps below. The intention is that the reader would implement the steps exactly as described here in order to obtain an effective DG limiter that integrates pressure positivity, applies nonlinear hybridization to the higher-order modes that reside in the faces, and finally produces a divergence-free zone-centered reconstruction for the magnetic field that is consistent with the facial modes of the magnetic field components. While the discussion below focuses on the novel aspects of MHD, it should be pointed out that the update of the fluid density, momentum density, and energy density is carried out entirely in accordance with a traditional DG scheme. Therefore, all aspects of obtaining fluid fluxes at the boundaries and the volume terms that are part of any traditional DG scheme for hydrodynamics will also apply to the zone-centered variables of any DG method for MHD. The steps are given below.

Step 1. In keeping with the philosophy of [10], we evolve all the zone-centered modes of all the conserved fluid variables using the finite-volume DG formulation. However, note that the conservation law includes the magnetic field components, for which we also have all the zone-centered modes. Flux evaluation and Riemann solvers cost the same regardless of whether they are evaluated for just the fluid variables or for the fluid plus magnetic field variables. Therefore, it adds almost nothing to the computational cost if the zone-centered magnetic field and its higher-order moments are also evolved in a DG sense. To summarize, the previous DG timestep has updated zone-centered fluid variables as well as zone-centered magnetic field variables. The face-centered modes of the DG scheme have also been updated by using the divergence-free formulation described in [13].

Step 2. It is very desirable to identify troubled zones in a DG calculation and handle those zones in a special way. Using Section 2.1 of [5] we build a flattener function within each zone. While the ideas extend to three dimensions, we illustrate them in two dimensions. Thus, for any zone (i, j) we build $f_{i,j}$, which is a flattener function that is built using (1) to (3) of Section 2.1 in [5].

Step 3. Using a characteristic-based TVD/TVB limiter, we limit all the zone-centered modes of the DG solution. This includes the zone-centered modes for the fluid variables and the zone-centered modes for the magnetic variables.

Step 4. Notice that the flattener $f_{i,j} \in [0, 1]$ by construction. If the zone is free of shocks, the flattener $f_{i,j}$ in that zone is zero and the modes that are given to us by the TVD/TVB limiting from the previous step are left untouched. As $f_{i,j}$ increases from zero, a factor of $(1 - f_{i,j})$ is multiplied to all the higher-order zone-centered modes (other than the mean value) in zone (i, j) . Those modes were given to us

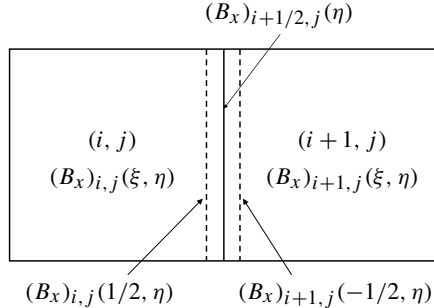


Figure 5. This figure shows how the limiting of facial modes is done by leveraging the zone-centered DG limiting. At each face we have three options that can be nonlinearly hybridized. We have the face-centered modes $(B_x)_{i+1/2,j}$ and from the zones that lie on either side of the face we also have zone-centered modes $(B_x)_{i,j}$ and $(B_x)_{i+1,j}$ that could contribute to the limiting of the facial modes as explained in the text.

by the TVD/TVB limiting in the previous step. In the few rare zones that are in a strong shock, or are about to be run over by a strong shock, the algorithm is such that $f_{i,j} = 1$ in those zones and the profile in those zones is completely flattened.

Step 5. We now have all the modes within each zone and now apply a positivity limiter following the ideas in [5; 72]. This involves scaling the higher modes of the solution so as to make it positive at a set of nodes which comes from quadrature rules. Therefore, notice that by this step, the nonlinear limiting and positivity-enforcement has been applied to all the fluid and magnetic variables within the zone. Admittedly, the magnetic field reconstruction is not divergence-free in this step, but that will be fixed in the next few steps.

Step 6. Now consider Figure 5. It shows two adjoining zones labeled (i, j) and $(i + 1, j)$. The zone boundary is labeled by $(i + 1/2, j)$. In each of those zones, we have a local coordinate system $(\xi, \eta) \in [-1/2, 1/2] \times [-1/2, 1/2]$. In the zone boundary $(i + 1/2, j)$ we also have a local coordinate $\eta \in [-1/2, 1/2]$. Now realize that we have three possible choices that we can use in the limiting the x component of the magnetic field $(B_x)_{i+1/2,j}(\eta)$ that resides in the face $(i + 1/2, j)$. Recall that this is the magnetic field component that is being evolved in constraint-preserving fashion. But from zone (i, j) we also have $(B_x)_{i,j}(1/2, \eta)$; please recall that this field has been nonlinearly limited in Step 3. Similarly, from zone $(i + 1, j)$ we also have $(B_x)_{i+1,j}(-1/2, \eta)$; realize that this field has also been nonlinearly limited in Step 3. So our limiting strategy for $(B_x)_{i+1/2,j}(\eta)$ should be such that when we have smooth flow, we strongly prefer that $(B_x)_{i+1/2,j}(\eta)$ should be unchanged after limiting. However, when either of the two neighboring zones contains a shock, we want the appropriate one-sided value. We would also like to use the flattener to suitably reduce the permitted variation at a face.

We now define our limiter as follows. We have the following set of profiles on the face $(i + 1/2, j)$, one from the face solution itself and two from the neighboring cells:

$$(B_x)_{i+1/2,j}(\eta) = \sum_{l=0}^k (a_l)_{i+1/2,j} \phi_l(\eta), \quad (B_x)_{i,j}(1/2, \eta) = \sum_{l=0}^k (a_l)_{i,j} \phi_l(\eta),$$

$$(B_x)_{i+1,j}(-1/2, \eta) = \sum_{l=0}^k (a_l)_{i+1,j} \phi_l(\eta)$$

and define the flattener parameters as

$$\bar{f}_{i,j} = 1 - f_{i,j}, \quad \bar{f}_{i+1,j} = 1 - f_{i+1,j}.$$

The facial modes are then modified using a minmod limiter as

$$(a_l)_{i+1/2,j}(\phi) \leftarrow \text{minmod}\left((a_l)_{i+1/2,j}, (1 + \beta \bar{f}_{i,j})(a_l)_{i,j}, (1 + \beta \bar{f}_{i+1,j})(a_l)_{i+1,j}\right)$$

for $l = 1, \dots, k$. The factor of $\beta \in [0, 1/2]$ in the above equation adds to a compression factor, and the reader is invited to see the analogy between the above equation and the compression factor in the well-known MC limiter. We see now that when the flow is smooth, we will tend to preferentially pick out $(B_x)_{i+1/2,j}(\eta)$ and the facial modes are left unchanged. When the modes are substantially smaller from one of the two zones that abut the face in question, the above formula will pick those smaller modes. Thus, the higher-order modes in a facial DG scheme are truly updated in a preferentially upwinded fashion. Moreover, the one-sided modes that are used in the above formula have been nonlinearly limited, so the nonlinear limiting of facial modes has been accomplished. This is how we limit the higher-order facial modes for the magnetic fields in a way that maximally leverages the zone-centered limiting. The mean magnetic flux at each face is left untouched because we do not limit the mode $(a_0)_{i+1/2,j}$ in the above formula, which is necessary to be able to perform the divergence-free reconstruction. This is done at all the faces of the skeleton mesh. We also note that this DG limiting for the faces is very general and applies naturally to isoparametrically mapped curvilinear meshes.

Step 7. Now that the higher-order facial modes for the magnetic fields have been limited, we can use them to obtain the divergence-free reconstruction within each zone. This indeed overwrites the mean zone-centered magnetic field components. In other words, the facial magnetic field variables are the primal variables of the scheme; therefore, they eventually reset the mean zone-centered magnetic field components at each substep in the scheme.

With these seven steps, the zone-centered fluid variables and the face-centered magnetic variables have been limited in a solution-adaptive fashion using TVD-based DG limiting. Positivity is closely integrated into the MHD limiting method.

The resulting reconstructed magnetic field is divergence-free. We are, therefore, ready to take the next substep (or the next step) in the RKDG scheme for MHD.

8. Troubled cell indicator

In the previous section, we have discussed the implementation of limiting strategy in the DG scheme for MHD. Applying the limiter uniformly over the whole domain may lead to smooth cells being limited mistakenly, especially at smooth extrema, which will reduce the accuracy of the solution in the smooth solution regions. It will be a good idea to identify the troubled cells first, and then the limiting strategy should be used for troubled cells only. There are many strategies available in the literature for detecting troubled cells; see e.g., [47; 30; 55]. Here, we consider the simple troubled cell indicator of Fu and Shu [38], who developed it in the DG framework for hyperbolic conservation laws and presented the results for the system of Euler equations. To identify if a target cell, denoted with \square_0 , is a troubled cell or not, we consider the stencil $S = \{\square_0, \square_1, \square_2, \square_3, \square_4\}$ as shown in [Figure 6](#). Let $\mathcal{U}_j(x, y)$ denote the polynomial solution of the conserved variables in the j -th cell and denote the cell average of this polynomial on the l -th cell as

$$\langle \mathcal{U}_j \rangle_l = \frac{1}{|\square_l|} \int_{\square_l} \mathcal{U}_j(x, y) dx dy, \quad 0 \leq j, l \leq 4.$$

The troubled cell indicator for the central cell \square_0 is defined as

$$I_{\square_0} := \frac{\sum_{j=1}^4 |\langle \mathcal{U}_j \rangle_0 - \langle \mathcal{U}_0 \rangle_0|}{\max_{j \in \{0, 1, 2, 3, 4\}} |\langle \mathcal{U}_j \rangle_j|}.$$

The cell is identified as a troubled cell if

$$I_{\square_0} > C_k$$

where C_k is a constant whose value is taken to be 0.5 in all the computations. We compute this indicator for each conserved variable and mark the cell as a troubled cell if any one of the components satisfies the above inequality. We found that the

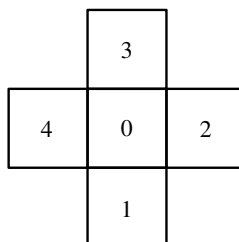


Figure 6. The stencil $S = \{\square_0, \square_1, \square_2, \square_3, \square_4\}$ for troubled cell indicator test.

indicator can be triggered in cases where the solution is constant and zero, but due to small numerical variations, it may not be exactly zero. This can happen, e.g., if the momentum or magnetic field is zero in some portion of the computational domain. To avoid such false identification, we first examine the linear moments of the polynomial solution which represent the solution gradients. If this is smaller than Mh^2 , then we conclude that the solution is constant in the current cell and mark it as not troubled; otherwise we compute the troubled cell indicator to decide its smoothness. In the computations, we choose $M = 1$.

9. Numerical results

We have explained the semidiscrete version of the DG scheme in the previous sections, which leads to a system of coupled ODEs. Starting from the specified initial condition, these ODEs are integrated forward in time using Runge–Kutta schemes. For $k = 1$ and $k = 2$, we use the two-stage, second-order and three-stage, third-order strong stability-preserving Runge–Kutta (SSPRK) schemes [61], respectively, while for $k = 3$ we use the five-stage, fourth-order SSPRK scheme. The timestep is computed as

$$\Delta t = \frac{\text{CFL}}{\max((|v_x| + c_{fx})/\Delta x + (|v_y| + c_{fy})/\Delta y)}$$

where c_{fx} , c_{fy} are the fastest wave speeds in the MHD eigensystem given by

$$c_{f\alpha} = \sqrt{\frac{1}{2}(c_s^2 + \mathbf{b}^2) + \frac{1}{2}\sqrt{(c_s^2 + \mathbf{b}^2)^2 - 4c_s^2 b_\alpha^2}}, \quad c_s = \sqrt{\frac{\gamma p}{\rho}}, \quad \mathbf{b} = \frac{\mathfrak{B}}{\sqrt{4\pi\rho}}.$$

Unless stated otherwise, in all the test cases we use $\text{CFL} = 0.95/(2k + 1)$, where k is the degree of the approximating polynomials. In all the test cases, we set the value of the adiabatic index to be $\gamma = \frac{5}{3}$ unless stated otherwise. A high-level view of the algorithm is given in [Algorithm 1](#).

The decreasing CFL number with increasing order of a DG scheme is a standard feature of all DG schemes. It arises from von Neumann stability analysis of DG schemes, as shown in [13]. At an intuitive level, one can think of a DG scheme as providing true physical evolution to all the modes. Consequently, DG schemes offer a kind of true subcell resolution. But if each DG zone is offering the effective resolution of multiple FV zones, then it is natural to expect the DG timestep to be much smaller than the FV timestep. For smooth solutions, high-order DG schemes yield an accurate solution with fewer number of zones, which compensates for the diminishing timestep.

9.1. Alfvén wave. Alfvén waves are linearly degenerate waves in the MHD system. As a result, they can propagate over long distances without dissipation or dispersion.

```

Allocate memory for all variables;
Set initial condition on the faces and cells;
Loop over cells and do divergence-free reconstruction;
 $t = 0$ ;
while  $t < T$  do
    Copy current solution into old solution;
    Compute timestep  $\Delta t$ ;
    for each RK stage do
        Loop over vertices: compute vertex flux using 2D Riemann solver;
        Loop over faces: compute all face integrals using flux from 1D Riemann solver;
        Loop over cells: compute all cell integrals;
        Update solution cell solution  $\mathcal{U}$ , face solution  $\mathbf{B}$  to next stage;
        Loop over cells: limit all cell variables  $\mathcal{U}$ ;
        Loop over faces: limit normal component  $\mathbf{B}$  using limited cell solution  $\mathcal{U}$ ;
        Loop over cells and perform divergence-free reconstruction;
        Apply positivity limiter;
    end
     $t = t + \Delta t$ ;
end

```

Algorithm 1. Exactly divergence-free scheme for ideal compressible MHD.

Such Alfvén waves also play a very important role in the development of MHD turbulence. As a result, this test shows that our progressively higher-order schemes are indeed capable of propagating Alfvén waves with increasing order of accuracy with the expected reduction of dissipation and dispersion that comes with increasing accuracy. This makes them suitable for turbulence applications.

The test case involves the propagation of a smooth circularly polarized Alfvén wave [64] and is used to test accuracy and convergence of numerical algorithms. The domain is taken to be $[0, 1/\cos \alpha] \times [0, 1/\sin \alpha]$ and α is the angle of wave propagation relative to the x axis whose value is taken to be $\frac{\pi}{6}$. We use periodic boundary conditions in both directions. The initial condition is given by

$$\begin{aligned} \rho &= 1, & \mathbf{v} &= v_{\perp}(-\sin \alpha, \cos \alpha, 0), & p &= 0.1, \\ B_x &= B_{\parallel} \cos \alpha - B_{\perp} \sin \alpha, & B_x &= B_{\parallel} \sin \alpha + B_{\perp} \cos \alpha, & B_z &= v_z, \end{aligned}$$

where

$$B_{\parallel} = 1, \quad B_{\perp} = v_{\perp} = 0.1 \sin(2\pi(x \cos \alpha + y \sin \alpha)).$$

The numerical solution is computed at time $T = \sqrt{4\pi}$ and $\gamma = \frac{5}{3}$. The convergence of the error for conservative variables with respect to grid refinement is shown in Figure 7, which indicates that the optimal rates of 2, 3, and 4 have been achieved for all the variables. Figure 7 seems to show a mild superconvergence in some variables and such superconvergence is also sometimes observed in other DG schemes.

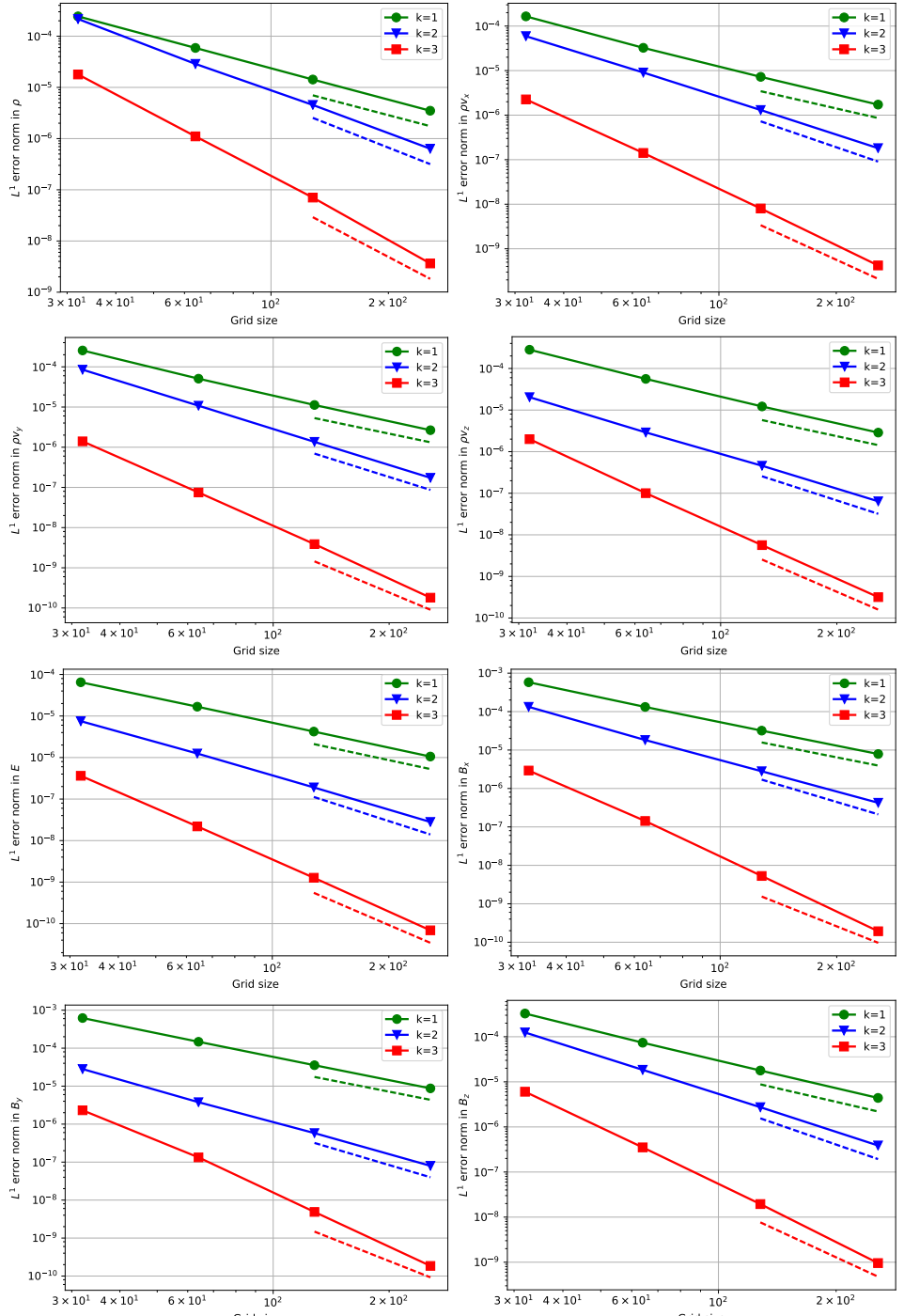


Figure 7. Convergence results for the smooth Alfvén wave problem. The dashed lines show second-, third-, and fourth-order rates.

9.2. Smooth magnetic vortex. There are very few multidimensional MHD test problems where a complicated flow structure propagates on the mesh with no change in form. This smooth vortex solution, which was invented by Balsara [2], is one of the best known examples. As a result, it is a very useful test problem for documenting the accuracy of an MHD scheme. The smooth vortex returns to its initial position after some fixed time period and allows us to measure the accuracy and convergence of the numerical algorithms. The problem is initialized over the computational domain $[-10, 10] \times [-10, 10]$ with periodic boundary conditions in both directions. The initial unperturbed primitive variables are given by

$$\rho = 1, \quad p = 1, \quad \mathbf{v} = (1, 1, 0), \quad \mathbf{B} = (0, 0, 0),$$

and $\gamma = \frac{5}{3}$. A vortex is initialized at the origin by adding the fluctuations in velocity and magnetic field, which are given by

$$\begin{aligned} \delta v_x &= -\frac{\kappa}{2\pi} y \exp(0.5(1-r^2)), & \delta v_y &= \frac{\kappa}{2\pi} x \exp(0.5(1-r^2)), & \delta v_z &= 0, \\ \delta B_x &= -\frac{\mu}{2\pi} y \exp(0.5(1-r^2)), & \delta B_y &= \frac{\mu}{2\pi} x \exp(0.5(1-r^2)), & \delta B_z &= 0, \end{aligned}$$

and the perturbation in pressure is

$$\delta p = \left[\frac{1}{8\pi} \left(\frac{\mu}{2\pi} \right)^2 (1-r^2) - \frac{1}{2} \left(\frac{\kappa}{2\pi} \right)^2 \right] \exp(1-r^2).$$

For the parameters in the initial condition, we set $\kappa = 1$ and $\mu = \sqrt{4\pi}$. The numerical solution is computed up to time $T = 20$. The convergence of the error for conservative variables with respect to grid refinement is shown in Figure 8, which indicates that the optimal rates of 2, 3, and 4 have been achieved for all the variables.

9.3. Brio–Wu shock tube. The MHD system is nonconvex with the result that it can produce compound shocks which are not present in the hydrodynamical setting. This was realized by Brio and Wu [20], who therefore constructed this very classical MHD test problem. The spike that is visible in density and transverse magnetic field represents a compound shock that is formed by an Alfvén wave and a slow rarefaction. The initial condition is a Riemann problem and has a discontinuity; for $x < 0$, the state is given by

$$\rho = 1, \quad p = 1, \quad \mathbf{v} = (0, 0, 0), \quad \mathbf{B} = \sqrt{4\pi}(0.75, 1, 0)$$

and for $x > 0$, it is given by

$$\rho = 0.125, \quad p = 0.1, \quad \mathbf{v} = (0, 0, 0), \quad \mathbf{B} = \sqrt{4\pi}(0.75, -1, 0).$$

The hydrodynamic variables are the same as the Sod shock tube problem. The solution of this problem contains a fast rarefaction wave, an intermediate shock

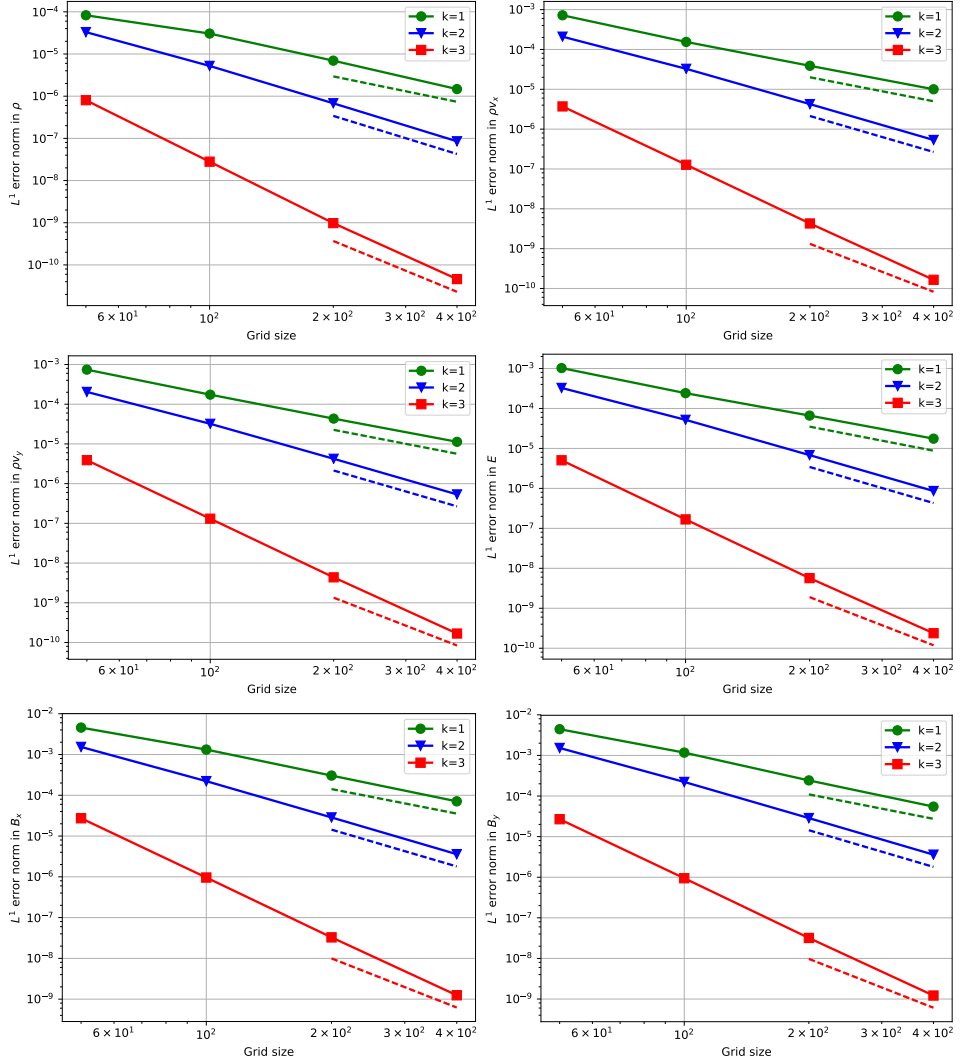


Figure 8. Convergence results for the smooth vortex problem. The dashed lines shows second-, third-, and fourth-order rates.

followed by a slow rarefaction wave, a contact discontinuity, a slow shock, and a fast rarefaction wave. We have computed the numerical solution for degrees $k = 1, 2, 3$ at time $T = 0.2$ using 800 cells. The value of γ is taken to be $\frac{5}{3}$. In Figure 9, we have compared the numerical solutions with the exact solutions from the Riemann solver of Torrilhon [62; 63]. We can observe from the figures that for all degrees our DG schemes are able to capture the discontinuities in a nonoscillatory manner.

9.4. Ryu–Jones shock tube problem. While the previous test problems show some of the unique features that are only present in MHD, this test problem shows a

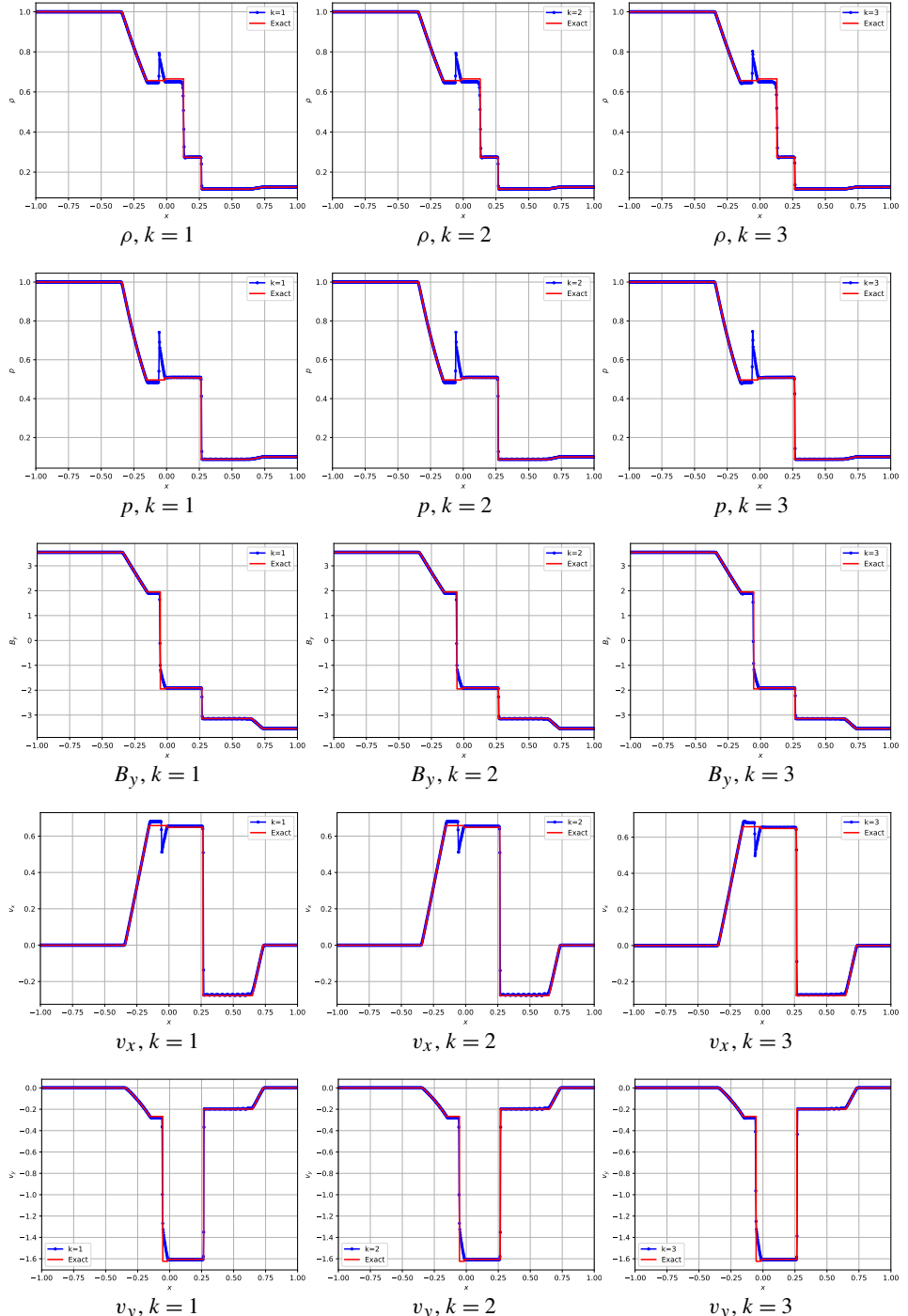


Figure 9. Comparison of numerical solutions obtained using $k = 1, 2, 3$ with the exact solution for Brio–Wu shock tube problem over a grid of 800 cells at time $T = 0.2$.

different feature about the MHD system. An analysis of the characteristic matrices for MHD shows that the system can sustain a seven-fold foliation of waves. The present Riemann problem was constructed by Ryu and Jones [58] and shows a problem with a left-going fast shock, a left-going Alfvén wave, a left-going slow shock, a contact discontinuity, a right-going slow shock, a right-going Alfvén wave, and a right-going fast wave. The foliation of waves from left to right in that sequence is visible in the simulations. The problem is solved in the domain $[-0.5, 0.5]$, where the initial condition has a discontinuity; for $x < 0$, the state is given by

$$\rho = 1.08, \quad p = 0.95, \quad \mathbf{v} = (1.2, 0, 0), \quad \mathbf{B} = (2, 3.6, 2)$$

and for $x > 0$, it is given by

$$\rho = 1, \quad p = 1, \quad \mathbf{v} = (0, 0, 0), \quad \mathbf{B} = (2, 4, 2).$$

The numerical solution is computed at time $T = 0.2$ and we use $\gamma = \frac{5}{3}$. In Figure 10, we have compared the numerical solutions for degrees $k = 1, 2, 3$ with the exact solution of Torrilhon [62; 63]. The proposed schemes resolve the discontinuities in a nonoscillatory manner.

9.5. Orszag–Tang vortex. MHD flows can indeed become turbulent, just like hydrodynamical flows. This test problem, which was constructed by Orszag and Tang [54], shows how an MHD flow that starts with a simple smooth flow profile can transition to a complex flow having many discontinuities and eventually leads to supersonic turbulent flow. It therefore illustrates the path that MHD flows can take as they become turbulent. Many MHD numerical schemes show instability for this problem if the divergence error is not controlled sufficiently during the simulations [48; 50]. This test case also motivates us to devise global divergence-free DG schemes as higher-order local divergence-free DG schemes also show instability with time [48]. Due to its complex structure and sensitivity to divergence errors, this test case is an important benchmark to demonstrate the robustness of numerical schemes for MHD.

Numerical simulations are performed over the domain $[0, 1] \times [0, 1]$ with periodic boundary conditions on all sides. The initial condition is given by

$$\begin{aligned} \rho &= \frac{25}{36\pi}, & p &= \frac{5}{12\pi}, \\ \mathbf{v} &= (-\sin(2\pi y), \sin(2\pi x), 0), & \mathbf{B} &= (-\sin(2\pi y), \sin(4\pi x), 0). \end{aligned}$$

The numerical solutions are computed up to the time $T = 0.5$ using grids of sizes 128×128 , 256×256 , and 512×512 . In Figure 11, we have shown the results for density obtained using second-, third-, and fourth-order schemes. We can visually observe that third- and fourth-order schemes resolve the solution better

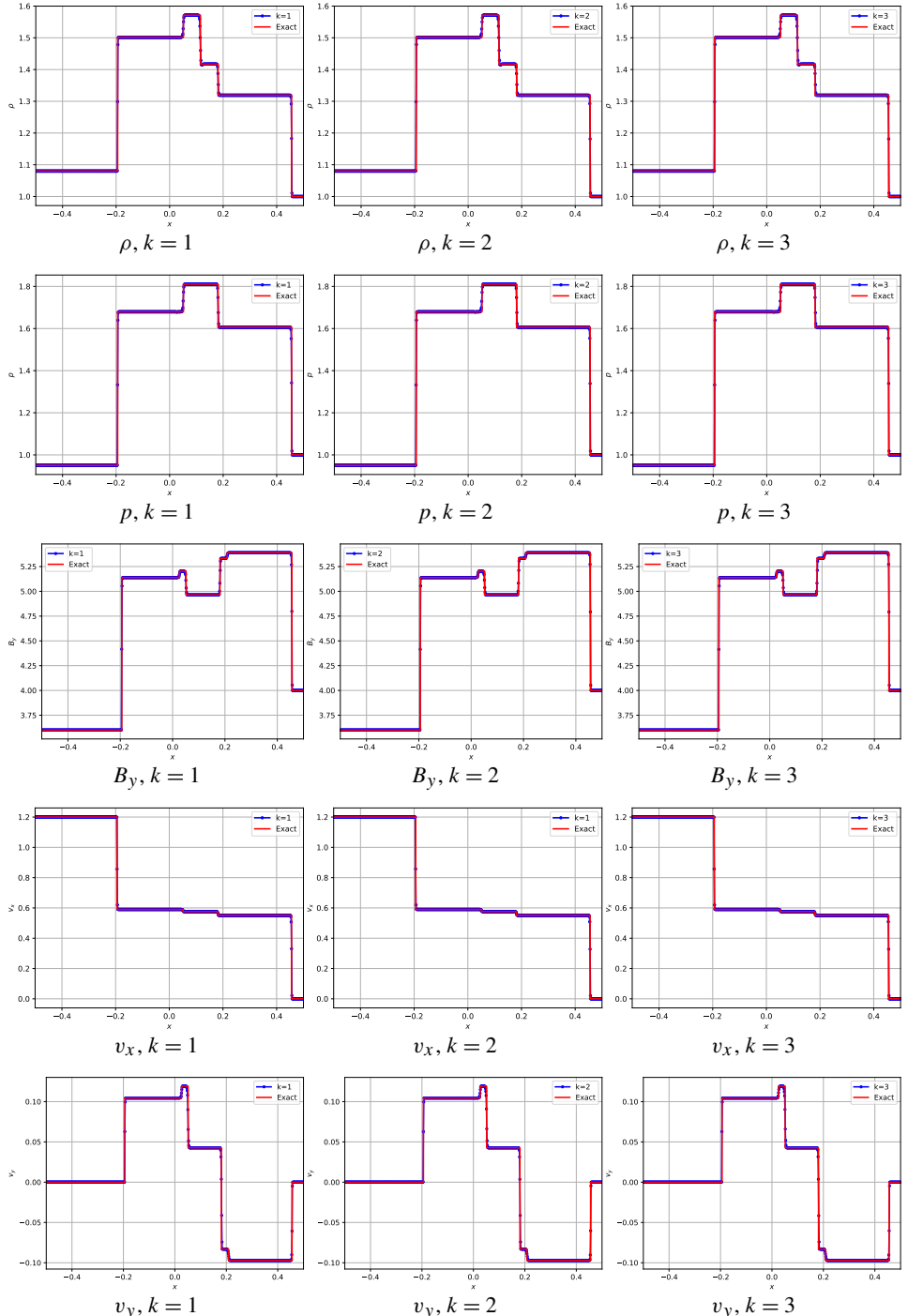


Figure 10. Comparison of numerical solutions obtained using $k = 1, 2, 3$ with the exact solution for Ryu–Jones problem over a grid of 800 cells at time $T = 0.2$.

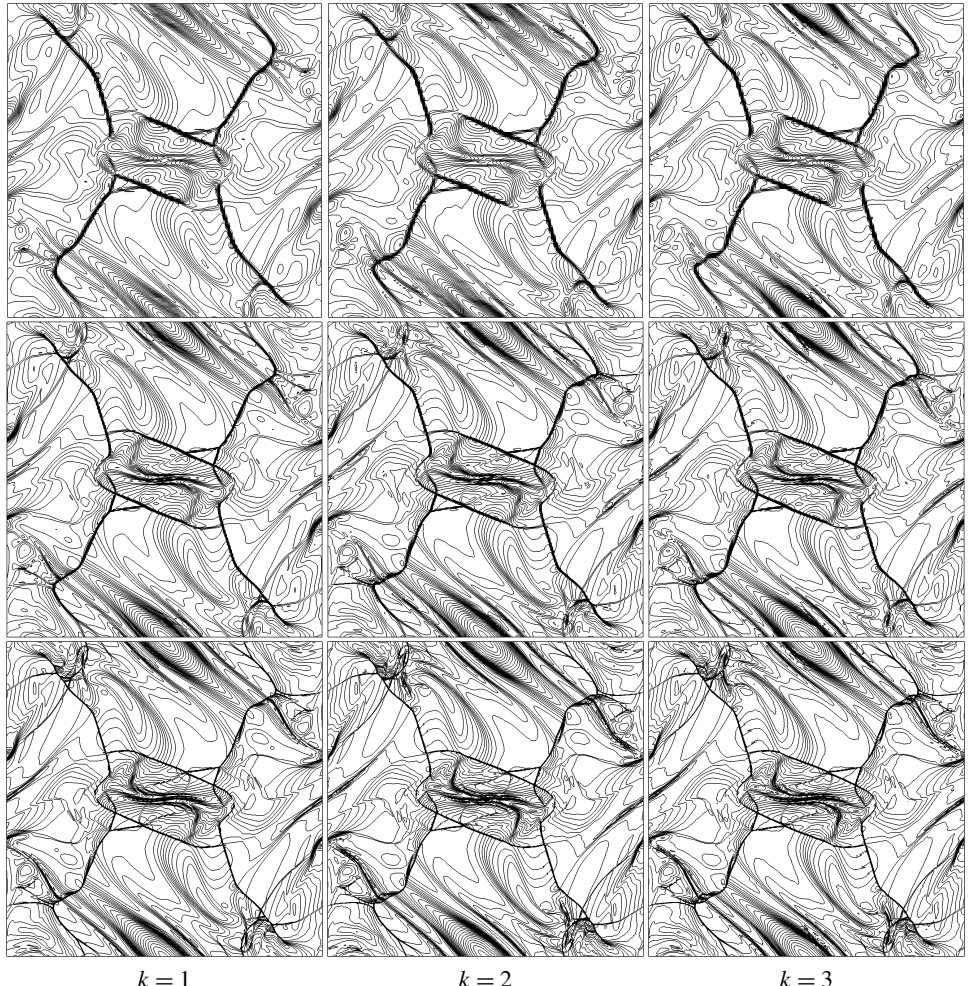


Figure 11. Orszag–Tang test using 128×128 (top row), 256×256 (middle row), and 512×512 (bottom row) meshes with TVD limiter and 30 density contours in $(0.08, 0.5)$.

in comparison to the second-order scheme, especially on the coarse grid of size 128×128 . The proposed schemes are able to resolve the small and large structures, and have a good agreement with the results in the literature [22; 48; 50].

9.6. Rotor test. Unlike hydrodynamic flows, MHD flows can be threaded by large-scale magnetic fields. The magnetic fields can sustain coherent, large-scale propagation of Alfvén waves, which can carry away angular momentum. Such a process cannot be achieved in hydrodynamical flows. In this test problem, a dense spinning cylinder that is threaded by an initially uniform magnetic field, is shown to cast off Alfvén waves and redistribute angular momentum in the process.

This test case was first proposed in [18], but we use the version given in [64], where it is referred to as the *first rotor problem*. This problem describes the spinning of a dense rotating disc of fluid in the center while the ambient fluid is at rest. The magnetic field wraps around the rotating dense fluid, turning it into an oblate shape. Distortions may develop in the solution if the numerical scheme does not sufficiently control the divergence error in the magnetic field [48].

The computational domain is $[0, 1] \times [0, 1]$ with periodic boundary conditions on all sides, and the initial condition is given as follows. For $r < r_0$,

$$\rho = 10, \quad \mathbf{v} = \frac{u_0}{r_0}(-(y - 1/2), (x - 1/2), 0),$$

and for $r_0 < r < r_1$

$$\rho = 1 + 9f, \quad \mathbf{v} = \frac{fu_0}{r}(-(y - 1/2), (x - 1/2), 0), \quad f = \frac{r_1 - r}{r_1 - r_0},$$

and for $r > r_1$

$$\rho = 1, \quad \mathbf{v} = (0, 0, 0)$$

with $r_0 = 0.1$, $r_1 = 0.115$, and $u_0 = 2$. The rest of the quantities are constant in the whole domain and given by

$$p = 1, \quad \mathfrak{B} = (5, 0, 0).$$

We set $\gamma = 1.4$, and the solution is computed up to the time $T = 0.15$ units. Numerical solutions are computed over the meshes of sizes 128×128 , 256×256 , and 512×512 . In Figure 12, we have shown the contour plots of Mach number for second-, third-, and fourth-order schemes. We can observe from the figures that in all cases, the circularly rotating velocity field in the central part is captured well. We found that the proposed DG schemes work well and have good agreement with the results in the literature [18; 64]. Furthermore, as we refine the grid, the solutions remain stable and the features are captured more crisply.

9.7. Blast wave test. In MHD flows, the gas pressure can indeed be substantially smaller than the magnetic pressure. Since both the thermal and magnetic energies contribute to the total energy density, it makes problems with strong magnetic fields very challenging to simulate. This challenge is exacerbated when strong shocks are present. This test problem is intended to highlight the robustness of the algorithm by showing a solution where strong shocks interact with configurations that are magnetically dominated.

The test problem was first described in [18]. It involves a low gas pressure with small plasma-beta $\beta = 2p/\|\mathfrak{B}\|^2$, which makes it very challenging for numerical schemes to simulate and is used as a benchmark to test the robustness of the numerical schemes. The computational domain is $[0, 1] \times [0, 1]$ with periodic

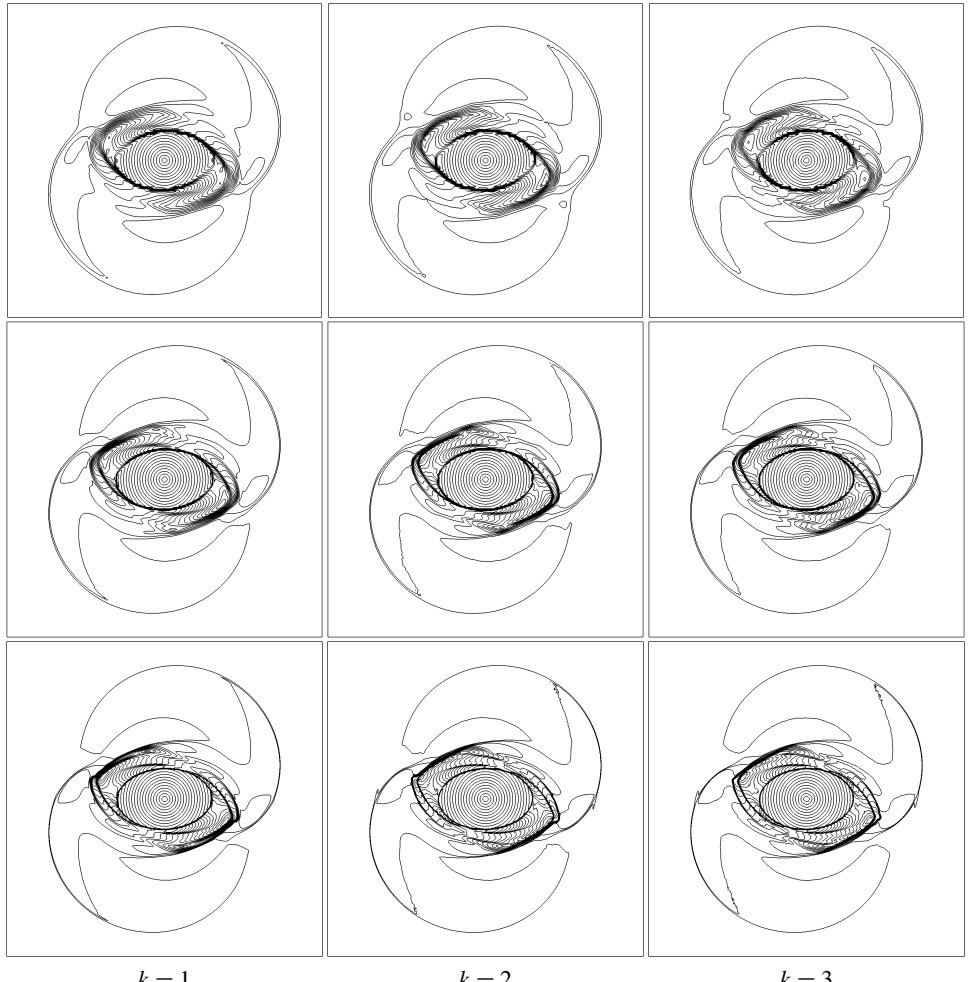


Figure 12. Rotor test using 128×128 mesh (top row), 256×256 mesh (middle row), and 512×512 mesh (bottom row) with TVD limiter and 20 Mach contours in $(0, 4.5)$.

boundary conditions on all sides. The problem is initialized with constant density, velocity, and magnetic field except the pressure. The initial condition has constant values of

$$\rho = 1, \quad \mathbf{v} = (0, 0, 0), \quad \mathbf{B} = (100, 0, 0)$$

in the whole domain, while the pressure is given by

$$p = \begin{cases} 1000, & r < 0.1, \\ 0.1, & r > 0.1, \end{cases} \quad \text{where } r^2 = (x - 0.5)^2 + (y - 0.5)^2.$$

The numerical computations are performed using a 200×200 grid and $\text{CFL} = 0.1$ up to the time $T = 0.01$. In Figures 13, 14, and 15, we have shown the density, the

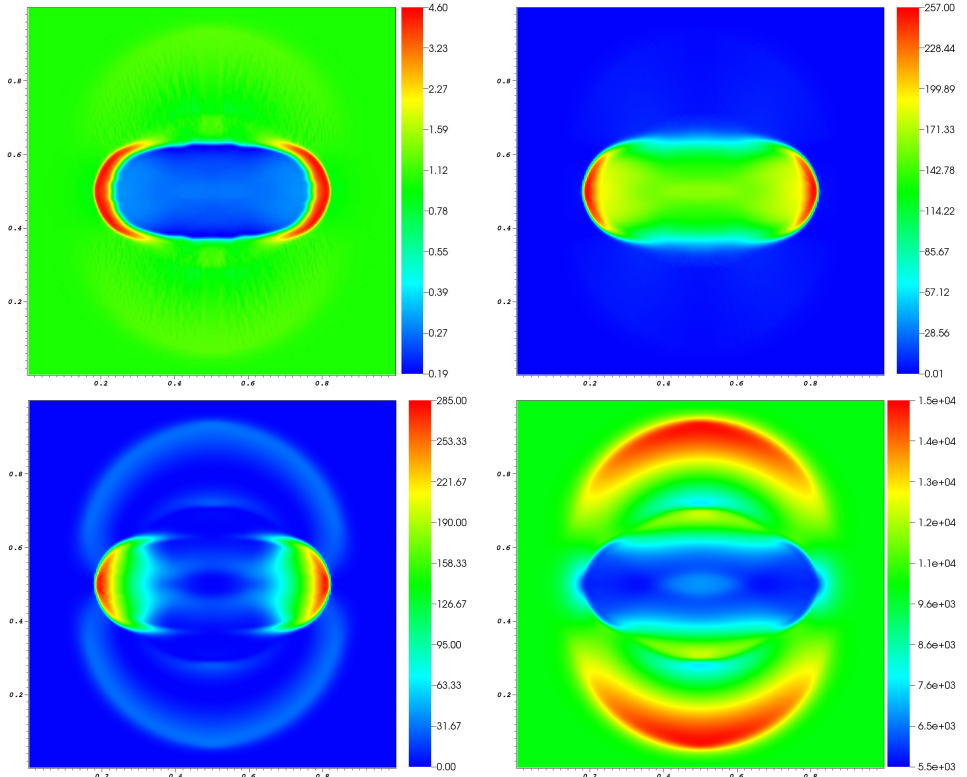


Figure 13. Blast test case using degree $k = 1$ on a 200×200 mesh and TVD limiter. Top left: $\log(\text{density})$. Top right: pressure. Bottom left: $v_x^2 + v_y^2$. Bottom right: $B_x^2 + B_y^2$.

pressure, $v_x^2 + v_y^2$, and $B_x^2 + B_y^2$ for the second, third, and fourth orders, respectively. We found that proposed DG schemes work in a robust manner and have good agreement with the results in literature [18; 2; 39]. Our results for the blast problem could be contrasted with Section 6.2.4 and Figures 12(b) and 14(b) of [39], which seem to generate unphysical solutions even at third order. The more meticulously designed DG schemes in this paper overcome the limitations of the DG schemes in the previous citation.

9.8. Magnetic field loop test. Sometimes the propagation of purely magnetic structures with strong discontinuities also presents a challenge to MHD simulation codes. Because the induction equation requires an update from the edge-centered electric field, the upwinding at the edges needs to include multidimensional effects. Therefore, this problem highlights the importance of multidimensional Riemann solvers in MHD.

The test case was introduced in [41] and involves the advection of a magnetic field loop over a periodic domain. The computational domain is $[-1, +1] \times [-0.5, +0.5]$

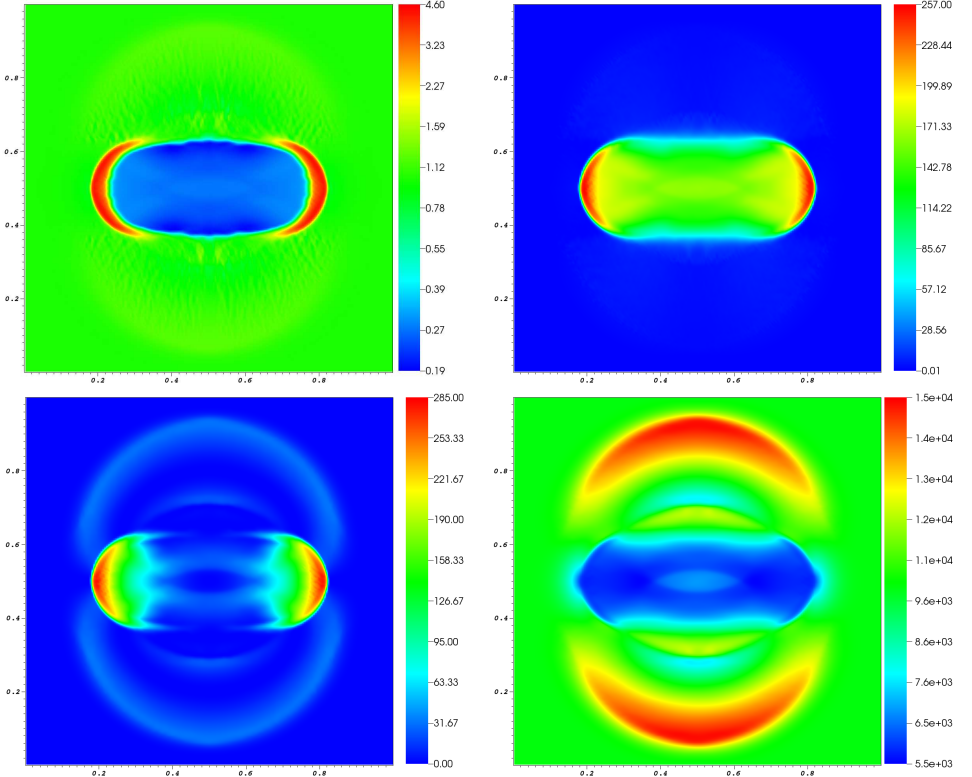


Figure 14. Blast test case using degree $k = 2$ on a 200×200 mesh and TVD limiter. Top left: $\log(\text{density})$. Top right: pressure. Bottom left: $v_x^2 + v_y^2$. Bottom right: $B_x^2 + B_y^2$.

with periodic boundary conditions in both directions. The initial density, pressure, and velocity are uniform in the domain and given by

$$\rho = 1, \quad p = 1, \quad \mathbf{v} = (2, 1, 0)$$

while the magnetic field is given by

$$\mathfrak{B} = \begin{cases} A_0(-y/r, x/r, 0), & r < r_0, \\ (0, 0, 0), & \text{otherwise.} \end{cases}$$

The parameters in the initial condition are $A_0 = \sqrt{4\pi} \times 10^{-3}$ and $r_0 = 0.3$, and the solution is computed up to a time of $T = 2$ units. In Figure 16, we have depicted the magnitude of magnetic pressure $\sqrt{B_x^2 + B_y^2}$ obtained using second-, third-, and fourth-order schemes over a 128×64 grid. The magnetic field loop advects over the domain and returns to its initial position. Since this solution is essentially linear advection of \mathbf{B} , the use of shock indicator as described in Section 8 is very critical to reduce the dissipation from limiters. We can observe the numerical dissipation

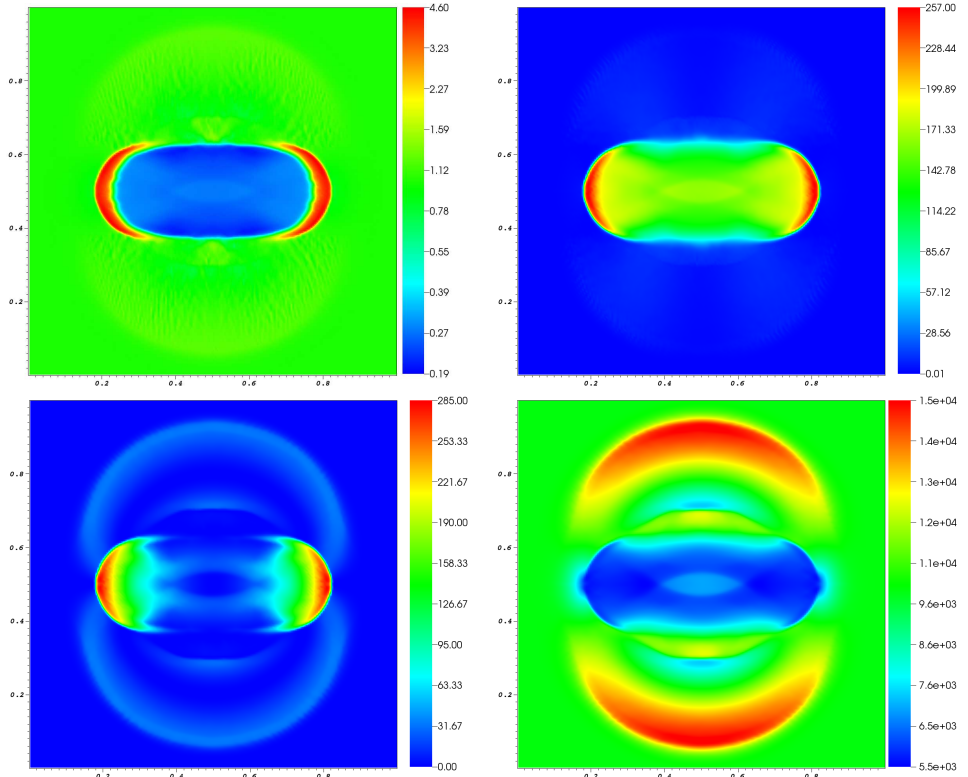


Figure 15. Blast test case using degree $k = 3$ on a 200×200 mesh and TVD limiter. Top left: $\log(\text{density})$. Top right: pressure. Bottom left: $v_x^2 + v_y^2$. Bottom right: $B_x^2 + B_y^2$.

around the center and boundary of the advected loop where the solution is less smooth and limiter is active. Reduction in the numerical dissipation can be observed as we go from second-order to higher-order schemes. The fourth-order scheme captures the loop with the least dissipation in comparison to second- and third-order DG schemes.

10. Summary and conclusions

In this paper we have presented a globally divergence-free DG scheme for ideal MHD that is based on the work of [13] and shown that it works robustly on even the most stringent of problems. Higher-order DG schemes are especially important in science and engineering because they offer low dissipation and dispersion as well as the ability to handle complex geometries. However, for the involution-constrained MHD equations, with their facially collocated magnetic fields, the DG schemes undergo substantial changes. The modes of the fluid variables are collocated at zone centers, and they form the primal variables of the fluid part of the DG scheme.

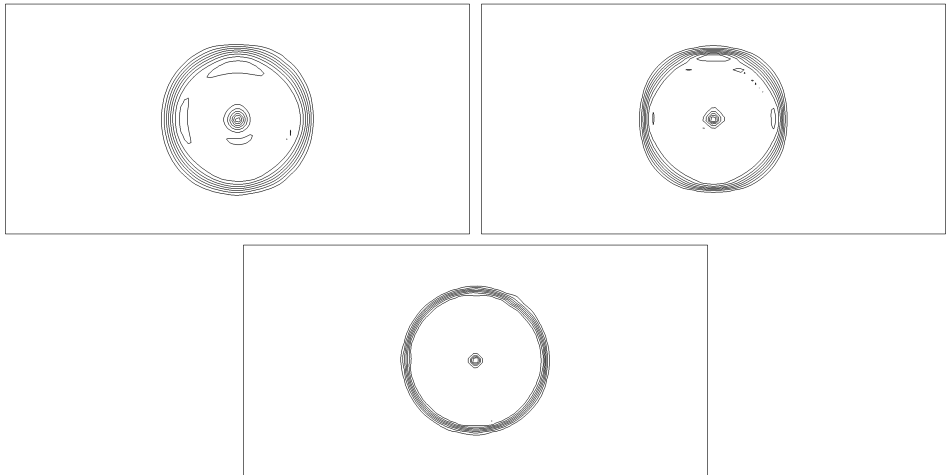


Figure 16. Contour plots of $\sqrt{B_x^2 + B_y^2}$ for the loop advection test using a 128×64 mesh at time $t = 2$; 10 contours are shown in the range $(0, 0.0042)$. Top left: $k = 1$. Top right: $k = 2$. Bottom: $k = 3$.

By contrast, the modes of the magnetic field components are collocated at the faces of the mesh, and they form the primal variables of the magnetic part of the DG scheme. While the fluid variables are evolved using a traditional DG scheme, a DG-like scheme from [13] is used for the globally divergence-free evolution of the magnetic field. By paying very careful attention to all aspects of scheme design, including limiting and positivity, we have been able to present up to fourth-order-accurate, globally constraint-preserving DG schemes that do not generate unphysical solutions.

The schemes that are presented in this paper rely on three essential building blocks. First, we use a divergence-free reconstruction of the magnetic field. Second, we use a weak-form, DG-like formulation of Faraday's law that is imposed in the faces of the mesh. Third, we rely on multidimensional Riemann solvers to provide a physically consistent electric field at the edges of the mesh. We also show that when we reach and exceed fourth-order accuracy, certain modes of the zonal magnetic field require a zone-centered evolution.

The MHD system is not just nonlinear but can also be nonconvex. This calls for the design of a robust and carefully designed limiter strategy for DG schemes for MHD. This paper delivers such a limiter strategy which retains the traditional DG limiting approach while building into it a positivity-enforcement step and a step that limits the facial modes in a constraint-preserving fashion. This limiter is crucial to the robust and physically consistent operation of our DG scheme for MHD even at high orders.

We have demonstrated that our DG schemes for MHD meet their design accuracies at second, third, and fourth orders. Our DG schemes are shown to robustly handle several stringent test problems.

In this paper we have shown how a full, working implementation of the globally divergence-free DG-like schemes of Balsara and Käppeli [13] can be achieved for the MHD equations. A robust formulation requires a good treatment of nonlinear limiting and positivity preservation. At fourth and higher orders, as realized by Balsara and Käppeli [13] themselves, a deft treatment of the reconstruction problem is needed, and such a treatment has been implemented in this paper and shown to work. These two advances also open the door to 3D implementations of the present DG-like schemes, and that will be the topic of a subsequent paper.

Acknowledgements

Balsara acknowledges support via National Science Foundation grants NSF-ACI-1533850, NSF-DMS-1622457, NSF-ACI-1713765, and NSF-DMS-1821242. A grant from Notre Dame International is also very gratefully acknowledged because it made possible the travel needed to complete this work. Kumar would like to acknowledge funding support from the National Post Doctoral Fellowship (PDF/2018/002621) administered by the Science and Engineering Research Board (SERB), Department of Science and Technology, Government of India. Chandrashekar would like to acknowledge support from the MATRICS project (MTR/2018/000006) of SERB and Department of Atomic Energy, Government of India, under project number 12-R&D-TFR-5.01-0520.

References

- [1] D. S. Balsara, *Divergence-free adaptive mesh refinement for magnetohydrodynamics*, J. Comput. Phys. **174** (2001), no. 2, 614–648. [Zbl](#)
- [2] ———, *Second-order-accurate schemes for magnetohydrodynamics with divergence-free reconstruction*, Astrophys. J. Suppl. S. **151** (2004), no. 1, 149–184.
- [3] ———, *Divergence-free reconstruction of magnetic fields and WENO schemes for magnetohydrodynamics*, J. Comput. Phys. **228** (2009), no. 14, 5040–5056. [MR](#) [Zbl](#)
- [4] ———, *Multidimensional HLLC Riemann solver: application to Euler and magnetohydrodynamic flows*, J. Comput. Phys. **229** (2010), no. 6, 1970–1993. [MR](#) [Zbl](#)
- [5] ———, *Self-adjusting, positivity preserving high order schemes for hydrodynamics and magnetohydrodynamics*, J. Comput. Phys. **231** (2012), no. 22, 7504–7517. [MR](#)
- [6] ———, *A two-dimensional HLLC Riemann solver for conservation laws: application to Euler and magnetohydrodynamic flows*, J. Comput. Phys. **231** (2012), no. 22, 7476–7503. [MR](#) [Zbl](#)
- [7] ———, *Multidimensional Riemann problem with self-similar internal structure, I: Application to hyperbolic conservation laws on structured meshes*, J. Comput. Phys. **277** (2014), 163–200. [MR](#) [Zbl](#)

- [8] ———, *Three dimensional HLL Riemann solver for conservation laws on structured meshes; application to Euler and magnetohydrodynamic flows*, J. Comput. Phys. **295** (2015), 1–23. [MR](#) [Zbl](#)
- [9] ———, *Higher-order accurate space-time schemes for computational astrophysics, I: Finite volume methods*, Living. Rev. Comput. Astrophys. **3** (2017), no. 1, art. id. 2.
- [10] D. S. Balsara and M. Dumbser, *Divergence-free MHD on unstructured meshes using high order finite volume schemes based on multidimensional Riemann solvers*, J. Comput. Phys. **299** (2015), 687–715. [MR](#) [Zbl](#)
- [11] ———, *Multidimensional Riemann problem with self-similar internal structure, II: Application to hyperbolic conservation laws on unstructured meshes*, J. Comput. Phys. **287** (2015), 269–292. [MR](#) [Zbl](#)
- [12] D. S. Balsara, M. Dumbser, and R. Abgrall, *Multidimensional HLLC Riemann solver for unstructured meshes: with application to Euler and MHD flows*, J. Comput. Phys. **261** (2014), 172–208. [MR](#) [Zbl](#)
- [13] D. S. Balsara and R. Käppeli, *Von Neumann stability analysis of globally divergence-free RKDG schemes for the induction equation using multidimensional Riemann solvers*, J. Comput. Phys. **336** (2017), 104–127. [MR](#) [Zbl](#)
- [14] ———, *Von Neumann stability analysis of globally constraint-preserving DGTD and PNPM schemes for the Maxwell equations using multidimensional Riemann solvers*, J. Comput. Phys. **376** (2019), 1108–1137. [MR](#) [Zbl](#)
- [15] D. S. Balsara, C. Meyer, M. Dumbser, H. Du, and Z. Xu, *Efficient implementation of ADER schemes for Euler and magnetohydrodynamical flows on structured meshes: speed comparisons with Runge–Kutta methods*, J. Comput. Phys. **235** (2013), 934–969. [MR](#) [Zbl](#)
- [16] D. S. Balsara and B. Nkonga, *Multidimensional Riemann problem with self-similar internal structure, III: A multidimensional analogue of the HLLI Riemann solver for conservative hyperbolic systems*, J. Comput. Phys. **346** (2017), 25–48. [MR](#) [Zbl](#)
- [17] D. S. Balsara, T. Rumpf, M. Dumbser, and C.-D. Munz, *Efficient, high accuracy ADER-WENO schemes for hydrodynamics and divergence-free magnetohydrodynamics*, J. Comput. Phys. **228** (2009), no. 7, 2480–2516. [MR](#) [Zbl](#)
- [18] D. S. Balsara and D. S. Spicer, *A staggered mesh algorithm using high order Godunov fluxes to ensure solenoidal magnetic fields in magnetohydrodynamic simulations*, J. Comput. Phys. **149** (1999), no. 2, 270–292. [MR](#) [Zbl](#)
- [19] S. H. Brecht, J. Lyon, J. A. Fedder, and K. Hain, *A simulation study of east-west IMF effects on the magnetosphere*, Geophys. Res. Lett. **8** (1981), no. 4, 397–400.
- [20] M. Brio and C. C. Wu, *An upwind differencing scheme for the equations of ideal magnetohydrodynamics*, J. Comput. Phys. **75** (1988), no. 2, 400–422. [MR](#) [Zbl](#)
- [21] P. Cargo and G. Gallice, *Roe matrices for ideal MHD and systematic construction of Roe matrices for systems of conservation laws*, J. Comput. Phys. **136** (1997), no. 2, 446–466. [MR](#) [Zbl](#)
- [22] P. Chandrashekar and C. Klingenberg, *Entropy stable finite volume scheme for ideal compressible MHD on 2-D Cartesian meshes*, SIAM J. Numer. Anal. **54** (2016), no. 2, 1313–1340. [MR](#) [Zbl](#)
- [23] Y. Cheng, F. Li, J. Qiu, and L. Xu, *Positivity-preserving DG and central DG methods for ideal MHD equations*, J. Comput. Phys. **238** (2013), 255–280. [MR](#) [Zbl](#)
- [24] A. J. Christlieb, X. Feng, Y. Jiang, and Q. Tang, *A high-order finite difference WENO scheme for ideal magnetohydrodynamics on curvilinear meshes*, SIAM J. Sci. Comput. **40** (2018), no. 4, A2631–A2666. [MR](#) [Zbl](#)

- [25] A. J. Christlieb, Y. Liu, Q. Tang, and Z. Xu, *Positivity-preserving finite difference weighted ENO schemes with constrained transport for ideal magnetohydrodynamic equations*, SIAM J. Sci. Comput. **37** (2015), no. 4, A1825–A1845. [MR](#) [Zbl](#)
- [26] A. J. Christlieb, J. A. Rossmanith, and Q. Tang, *Finite difference weighted essentially non-oscillatory schemes with constrained transport for ideal magnetohydrodynamics*, J. Comput. Phys. **268** (2014), 302–325. [MR](#) [Zbl](#)
- [27] B. Cockburn, S. Hou, and C.-W. Shu, *The Runge–Kutta local projection discontinuous Galerkin finite element method for conservation laws, IV: The multidimensional case*, Math. Comp. **54** (1990), no. 190, 545–581. [MR](#) [Zbl](#)
- [28] B. Cockburn and C.-W. Shu, *TVB Runge–Kutta local projection discontinuous Galerkin finite element method for conservation laws, II: General framework*, Math. Comp. **52** (1989), no. 186, 411–435. [MR](#) [Zbl](#)
- [29] ———, *The Runge–Kutta discontinuous Galerkin method for conservation laws, V: Multidimensional systems*, J. Comput. Phys. **141** (1998), no. 2, 199–224. [MR](#) [Zbl](#)
- [30] P. Colella and M. D. Sekora, *A limiter for PPM that preserves accuracy at smooth extrema*, J. Comput. Phys. **227** (2008), no. 15, 7069–7076. [MR](#) [Zbl](#)
- [31] W. Dai and P. R. Woodward, *On the divergence-free condition and conservation laws in numerical simulations for supersonic magnetohydrodynamical flows*, Astrophys. J. **494** (1998), no. 1, 317–335.
- [32] C. R. DeVore, *Flux-corrected transport techniques for multidimensional compressible magnetohydrodynamics*, J. Comput. Phys. **92** (1991), no. 1, 142–160. [Zbl](#)
- [33] S. Do, H. Li, and M. Kang, *Wavelet-based adaptation methodology combined with finite difference WENO to solve ideal magnetohydrodynamics*, J. Comput. Phys. **339** (2017), 482–499. [MR](#) [Zbl](#)
- [34] M. Dumbser and D. S. Balsara, *A new efficient formulation of the HLLEM Riemann solver for general conservative and non-conservative hyperbolic systems*, J. Comput. Phys. **304** (2016), 275–319. [MR](#) [Zbl](#)
- [35] M. Dumbser, D. S. Balsara, E. F. Toro, and C.-D. Munz, *A unified framework for the construction of one-step finite volume and discontinuous Galerkin schemes on unstructured meshes*, J. Comput. Phys. **227** (2008), no. 18, 8209–8253. [MR](#) [Zbl](#)
- [36] M. Dumbser, O. Zanotti, A. Hidalgo, and D. S. Balsara, *ADER-WENO finite volume schemes with space-time adaptive mesh refinement*, J. Comput. Phys. **248** (2013), 257–286. [MR](#) [Zbl](#)
- [37] C. R. Evans and J. F. Hawley, *Simulation of magnetohydrodynamic flows: a constrained transport method*, Astrophys. J. **332** (1988), 659–677.
- [38] G. Fu and C.-W. Shu, *A new troubled-cell indicator for discontinuous Galerkin methods for hyperbolic conservation laws*, J. Comput. Phys. **347** (2017), 305–327. [MR](#) [Zbl](#)
- [39] P. Fu, F. Li, and Y. Xu, *Globally divergence-free discontinuous Galerkin methods for ideal magnetohydrodynamic equations*, J. Sci. Comput. **77** (2018), no. 3, 1621–1659. [MR](#) [Zbl](#)
- [40] F. G. Fuchs, A. D. McMurry, S. Mishra, N. H. Risebro, and K. Waagan, *Approximate Riemann solvers and robust high-order finite volume schemes for multi-dimensional ideal MHD equations*, Commun. Comput. Phys. **9** (2011), no. 2, 324–362. [MR](#) [Zbl](#)
- [41] T. A. Gardiner and J. M. Stone, *An unsplit Godunov method for ideal MHD via constrained transport*, J. Comput. Phys. **205** (2005), no. 2, 509–539. [MR](#) [Zbl](#)
- [42] ———, *An unsplit Godunov method for ideal MHD via constrained transport in three dimensions*, J. Comput. Phys. **227** (2008), no. 8, 4123–4141. [MR](#) [Zbl](#)

- [43] K. F. Gurski, *An HLLC-type approximate Riemann solver for ideal magnetohydrodynamics*, SIAM J. Sci. Comput. **25** (2004), no. 6, 2165–2187. MR Zbl
- [44] A. Hazra, P. Chandrashekhar, and D. S. Balsara, *Globally constraint-preserving FR/DG scheme for Maxwell's equations at all orders*, J. Comput. Phys. **394** (2019), 298–328. MR
- [45] C. Helzel, J. A. Rossmanith, and B. Taetz, *An unstaggered constrained transport method for the 3D ideal magnetohydrodynamic equations*, J. Comput. Phys. **230** (2011), no. 10, 3803–3829. MR Zbl
- [46] ———, *A high-order unstaggered constrained-transport method for the three-dimensional ideal magnetohydrodynamic equations based on the method of lines*, SIAM J. Sci. Comput. **35** (2013), no. 2, A623–A651. Zbl
- [47] L. Krivodonova, J. Xin, J.-F. Remacle, N. Chevaugeon, and J. E. Flaherty, *Shock detection and limiting with discontinuous Galerkin methods for hyperbolic conservation laws*, Appl. Numer. Math. **48** (2004), no. 3–4, 323–338. MR Zbl
- [48] F. Li and C.-W. Shu, *Locally divergence-free discontinuous Galerkin methods for MHD equations*, J. Sci. Comput. **22–23** (2005), 413–442. MR Zbl
- [49] F. Li and L. Xu, *Arbitrary order exactly divergence-free central discontinuous Galerkin methods for ideal MHD equations*, J. Comput. Phys. **231** (2012), no. 6, 2655–2675. MR Zbl
- [50] F. Li, L. Xu, and S. Yakovlev, *Central discontinuous Galerkin methods for ideal MHD equations with the exactly divergence-free magnetic field*, J. Comput. Phys. **230** (2011), no. 12, 4828–4847. MR Zbl
- [51] S. Li, *An HLLC Riemann solver for magneto-hydrodynamics*, J. Comput. Phys. **203** (2005), no. 1, 344–357. MR Zbl
- [52] P. Londrillo and L. Del Zanna, *On the divergence-free condition in Godunov-type schemes for ideal magnetohydrodynamics: the upwind constrained transport method*, J. Comput. Phys. **195** (2004), no. 1, 17–48. MR Zbl
- [53] T. Miyoshi and K. Kusano, *A multi-state HLL approximate Riemann solver for ideal magnetohydrodynamics*, J. Comput. Phys. **208** (2005), no. 1, 315–344. MR Zbl
- [54] S. A. Orszag and C.-M. Tang, *Small-scale structure of two-dimensional magnetohydrodynamic turbulence*, J. Fluid Mech. **90** (1979), no. 1, 129–143.
- [55] P.-O. Persson and J. Peraire, *Sub-cell shock capturing for discontinuous Galerkin methods*, 44th AIAA Aerospace Sciences Meeting and Exhibit, American Institute of Aeronautics and Astronautics, Reston, VA, 2006.
- [56] P. L. Roe and D. S. Balsara, *Notes on the eigensystem of magnetohydrodynamics*, SIAM J. Appl. Math. **56** (1996), no. 1, 57–67. MR Zbl
- [57] J. A. Rossmanith, *An unstaggered, high-resolution constrained transport method for magnetohydrodynamic flows*, SIAM J. Sci. Comput. **28** (2006), no. 5, 1766–1797. MR Zbl
- [58] D. Ryu and T. W. Jones, *Numerical magnetohydrodynamics in astrophysics: algorithm and tests for one-dimensional flow*, Astrophys. J. **442** (1995), 228–258.
- [59] D. Ryu, F. Miniati, T. W. Jones, and A. Frank, *A divergence-free upwind code for multidimensional magnetohydrodynamic flows*, Astrophys. J. **509** (1998), no. 1, 244–255.
- [60] Y. Shen, G. Zha, and M. A. Huerta, *E-CUSP scheme for the equations of ideal magnetohydrodynamics with high order WENO scheme*, J. Comput. Phys. **231** (2012), no. 19, 6233–6247. MR
- [61] C.-W. Shu and S. Osher, *Efficient implementation of essentially nonoscillatory shock-capturing schemes*, J. Comput. Phys. **77** (1988), no. 2, 439–471. MR Zbl

- [62] M. Torrilhon, *Exact solver and uniqueness conditions for Riemann problems of ideal magnetohydrodynamics*, research report 2002-06, Seminar für Angewandte Mathematik, ETH Zürich, 2002.
- [63] ———, *Uniqueness conditions for Riemann problems of ideal magnetohydrodynamics*, J. Plasma Phys. **69** (2003), no. 3, 253–276. [Zbl](#)
- [64] G. Tóth, *The $\nabla \cdot B = 0$ constraint in shock-capturing magnetohydrodynamics codes*, J. Comput. Phys. **161** (2000), no. 2, 605–652. [MR](#) [Zbl](#)
- [65] A. R. Winters, D. Derigs, G. J. Gassner, and S. Walch, *A uniquely defined entropy stable matrix dissipation operator for high Mach number ideal MHD and compressible Euler simulations*, J. Comput. Phys. **332** (2017), 274–289. [MR](#) [Zbl](#)
- [66] A. R. Winters and G. J. Gassner, *Affordable, entropy conserving and entropy stable flux functions for the ideal MHD equations*, J. Comput. Phys. **304** (2016), 72–108. [MR](#) [Zbl](#)
- [67] Z. Xu, D. S. Balsara, and H. Du, *Divergence-free WENO reconstruction-based finite volume scheme for solving ideal MHD equations on triangular meshes*, Commun. Comput. Phys. **19** (2016), no. 4, 841–880. [MR](#) [Zbl](#)
- [68] S. Yakovlev, L. Xu, and F. Li, *Locally divergence-free central discontinuous Galerkin methods for ideal MHD equations*, J. Comput. Sci. **4** (2013), no. 1–2, 80–91. [Zbl](#)
- [69] K. Yee, *Numerical solution of initial boundary value problems involving Maxwell's equations in isotropic media*, IEEE Trans. Antennas Propagat. **14** (1966), no. 3, 302–307. [Zbl](#)
- [70] A. L. Zachary and P. Colella, *A higher-order godunov method for the equations of ideal magnetohydrodynamics*, J. Comput. Phys. **99** (1992), no. 2, 341–347. [Zbl](#)
- [71] A. L. Zachary, A. Malagoli, and P. Colella, *A higher-order Godunov method for multidimensional ideal magnetohydrodynamics*, SIAM J. Sci. Comput. **15** (1994), no. 2, 263–284. [MR](#) [Zbl](#)
- [72] X. Zhang and C.-W. Shu, *On positivity-preserving high order discontinuous Galerkin schemes for compressible Euler equations on rectangular meshes*, J. Comput. Phys. **229** (2010), no. 23, 8918–8934. [MR](#) [Zbl](#)

Received June 11, 2020. Revised December 8, 2020.

DINSHAW S. BALSARA: dbalsara@nd.edu

Department of Physics, University of Notre Dame, Notre Dame, IN, United States

RAKESH KUMAR: rakesh@tifrbng.res.in

Centre for Applicable Mathematics, Tata Institute of Fundamental Research, Bangalore, India

PRAVEEN CHANDRASHEKAR: praveen@tifrbng.res.in

Centre for Applicable Mathematics, Tata Institute of Fundamental Research, Bangalore, India

Communications in Applied Mathematics and Computational Science

msp.org/camcos

EDITORS

MANAGING EDITOR

John B. Bell

Lawrence Berkeley National Laboratory, USA

jbbell@lbl.gov

BOARD OF EDITORS

Marsha Berger	New York University berger@cs.nyu.edu	Ahmed Ghoniem	Massachusetts Inst. of Technology, USA ghoniem@mit.edu
Alexandre Chorin	University of California, Berkeley, USA chorin@math.berkeley.edu	Raz Kupferman	The Hebrew University, Israel raz@math.huji.ac.il
Phil Colella	Lawrence Berkeley Nat. Lab., USA pcolella@lbl.gov	Randall J. LeVeque	University of Washington, USA rjl@amath.washington.edu
Peter Constantin	University of Chicago, USA const@cs.uchicago.edu	Mitchell Luskin	University of Minnesota, USA luskin@umn.edu
Maksymilian Dryja	Warsaw University, Poland maksymilian.dryja@acn.waw.pl	Yvon Maday	Université Pierre et Marie Curie, France maday@ann.jussieu.fr
M. Gregory Forest	University of North Carolina, USA forest@amath.unc.edu	James Sethian	University of California, Berkeley, USA sethian@math.berkeley.edu
Leslie Greengard	New York University, USA greengard@cims.nyu.edu	Juan Luis Vázquez	Universidad Autónoma de Madrid, Spain juanluis.vazquez@uam.es
Rupert Klein	Freie Universität Berlin, Germany rupert.klein@pik-potsdam.de	Alfio Quarteroni	Politecnico di Milano, Italy alfio.quarteroni@polimi.it
Nigel Goldenfeld	University of Illinois, USA nigel@uiuc.edu	Eitan Tadmor	University of Maryland, USA etadmor@scamm.umd.edu
		Denis Talay	INRIA, France denis.talay@inria.fr

PRODUCTION

production@msp.org

Silvio Levy, Scientific Editor

See inside back cover or msp.org/camcos for submission instructions.

The subscription price for 2021 is US \$110/year for the electronic version, and \$165/year (+\$15, if shipping outside the US) for print and electronic. Subscriptions, requests for back issues from the last three years and changes of subscriber address should be sent to MSP.

Communications in Applied Mathematics and Computational Science (ISSN 2157-5452 electronic, 1559-3940 printed) at Mathematical Sciences Publishers, 798 Evans Hall #3840, c/o University of California, Berkeley, CA 94720-3840, is published continuously online. Periodical rate postage paid at Berkeley, CA 94704, and additional mailing offices.

CAMCoS peer review and production are managed by EditFLOW® from MSP.

PUBLISHED BY

 **mathematical sciences publishers**

nonprofit scientific publishing

<http://msp.org/>

© 2021 Mathematical Sciences Publishers

Communications in Applied Mathematics and Computational Science

vol. 16

no. 1

2021

From interacting agents to density-based modeling with stochastic PDEs Luzie Helfmann, Nataša Djurdjevac Conrad, Ana Djurdjevac, Stefanie Winkelmann and Christof Schütte	1
Stochastic parametrization with VARX processes Nick Verheul and Daan Crommelin	33
Globally divergence-free DG scheme for ideal compressible MHD Dinshaw S. Balsara, Rakesh Kumar and Praveen Chandrashekhar	59
Spectral steady-state solutions to the 2D compressible Euler equations for cross-mountain flows Jorge E. Guerra and Paul A. Ullrich	99
Balanced data assimilation for highly oscillatory mechanical systems Gottfried Hastermann, Maria Reinhardt, Rupert Klein and Sebastian Reich	119